



HAL
open science

Thermo-mechanical behavior of large ash-flow calderas

Evgenii E.B. Burov, Laurent Guillou-Frottier

► **To cite this version:**

Evgenii E.B. Burov, Laurent Guillou-Frottier. Thermo-mechanical behavior of large ash-flow calderas. *Journal of Geophysical Research: Solid Earth*, 1999, 104 (B10), pp.23081-23109. 10.1029/1999JB900227 . hal-00562364

HAL Id: hal-00562364

<https://brgm.hal.science/hal-00562364>

Submitted on 8 Feb 2021

HAL is a multi-disciplinary open access archive for the deposit and dissemination of scientific research documents, whether they are published or not. The documents may come from teaching and research institutions in France or abroad, or from public or private research centers.

L'archive ouverte pluridisciplinaire **HAL**, est destinée au dépôt et à la diffusion de documents scientifiques de niveau recherche, publiés ou non, émanant des établissements d'enseignement et de recherche français ou étrangers, des laboratoires publics ou privés.

Thermomechanical behavior of large ash flow calderas

Evgenii B. Burov¹ and Laurent Guillou-Frottier

Geology and Metallogeny Laboratory, BRGM, Orléans, France

Abstract. The fundamental thermal and mechanical processes that occur within the “ash flow caldera-magma chamber” systems remain largely enigmatic. To date, the only models of caldera collapse are simple, mostly elastic or viscoelastic mechanical models that can predict some of the conditions preceding the collapse. They cannot, however, predict the collapse itself because they are incapable either of reproducing the formation of faults or of accounting for the brittle-ductile transitions and fault-related thermal anomalies. We have constructed analytical and numerical thermomechanical models that account for both elastic-plastic-ductile rheology and physical properties of the caldera rocks. The overpressured magma is evacuated through a central vent and transforms into ash flow units deposited within the forming caldera. Brittle deformation, faulting, and subsequent collapse of the structure are reproduced. The results show that in the absence of a regional stress field the collapse on both sides will occur only for aspect ratios (i.e., caldera diameter to the depth of the magma chamber) exceeding 5 and that internal embedded faults may also appear when the aspect ratio exceeds 10. Thermal conductivity contrasts in ash flow calderas give rise to strong heat refraction that localizes deep seated thermal anomalies to the outer sides of the faults. In the presence of regional extension the border faulting can be attenuated or disappear, and the faults tend to localize around the central part of the chamber roof. Coupled thermomechanical modeling suggests that the outer sides of the border faults have high trapping capabilities for hydrothermal fluids. The geometry of the brittle-ductile transition largely controls that of the fractured zones within and around the chamber roof, thus justifying a new “mechanical definition” of magma chamber geometry.

1. Introduction

Growing interest in the exploration potential of ash flow calderas has stimulated numerous modeling studies that are mostly focused on fluid flow problems such as localized hydrothermal circulation through the intensive fracture networks typically formed in the magma chamber roof and around the border faults. However, recent studies in related research fields (for example, modeling of mineralized fluid flow in sedimentary basins) have demonstrated the necessity of taking into account stress, fracture, and temperature evolution within the whole tectonic unit involved because these can impose critical conditions on localized fluid circulation. Yet many processes taking place in magmatic systems, including the initiation of border faulting, mechanisms of caldera collapse, and related changes in the thermal and stress field, are still poorly investigated, al-

though they present quite important geodynamic problems.

Ash flow (or ignimbrite) calderas are thought to form when large eruptions remove tremendous quantities of magma from shallow silicic magma chambers beneath volcanic cones. During a major eruption, which commonly destroys the volcanic structure, the amount of extruded magma may be so important that the resulting mass deficit in the chamber, combined with the weight of the overlying surface ash flow deposits, leads to the inward collapse of the chamber roof and to the formation of a caldera.

Studies on ash flow calderas over the past half century have mostly focused on mineralogy, petrology, and structural geology [Williams, 1941; Smith, 1960; Steven and Lipman, 1976], complemented by only a few, chiefly conceptual, models of caldera formation and evolution [Smith and Bailey, 1968]. Although a number of simplified mechanisms of caldera formation have been suggested and investigated since the 1970s [e.g., Druitt and Sparks, 1984], the processes leading to various types of ash flow caldera or different subsidence styles imply many parameters that are difficult to include in a single scheme: caldera diameter, volume of ejected material, geometry of the magma chamber, refeeding or cooling of

¹Now at Tectonics Department, University of Pierre and Marie Curie, Paris, France

the magma reservoir, regional stress field, erosion rate, etc.

The recent review by *Lipman* [1997] proposed five end-member subsidence scenarios (Figure 1) for calderas: Figure 1a, "plate" or "piston-like"; Figure 1b, "piecemeal"; Figure 1c, "trapdoor"; Figure 1d, "downsag"; and Figure 1e, "funnel". According to this classification, the plate or piston-like subsidence is associated with large calderas formed by voluminous eruptions

from large shallow magma chambers, whereas the trapdoor subsidence could derive from smaller eruptions, associated with an asymmetrical magma chamber or with a regional tectonic regime. Funnel calderas are associated with small-scale (< 2-4 km) structures that would develop in relatively weak crusts. The great diversity of ash flow caldera types is difficult to interpret from field observations only, because one can imagine several independent mechanisms that could produce a similar collapse scenario; the physical links between the subcrustal processes and their surface expression have not really been investigated.

Most recent large-scale thermomechanical modeling studies of caldera evolution have either considered rather simplified scenarios based on the elastic and viscous rheologies [e.g., *Luongo et al.*, 1991; *Gudmundsson et al.*, 1997] often originating from some older and not quite self-consistent studies, or they have been focused on problems related to magma chamber emplacement and surface deformation. Some of these models [e.g., *De Natale et al.*, 1997; *Gudmundsson et al.*, 1997] predict stress concentrations at the borders of the magma chamber, which are anticipated to coincide with zones of fault initialization. None of the existing numerical and analytical models treats the problem of the initiation and evolution of border faults around the magma chamber in a mechanically consistent way, i.e., using realistic rock rheologies and without predefining fault surfaces or weakness planes. *Gudmundsson et al.* [1997], for example, attempt to predict the location and initiation conditions of the border faults by modeling stress concentrations at the corners of the magma chamber, but the elastic rheology and small-strain boundary element method that they used can give only hints, hardly real solutions. This point has recently been discussed in a number of studies that warn against a direct application of pure elastic or viscous solutions for predicting brittle failure zones [e.g., *Buck*, 1997; *Gerbault et al.*, 1998].

A few geophysical models have been proposed to investigate the dynamics of large shallow calderas. One of them, a two-stage model by *Druitt and Sparks* [1984], gives a simplified analysis of the relationships between the erupted volumes and magma chamber pressures. Another, a numerical model by *Chéry et al.* [1991], can be considered at present as the most complete because it is based on temperature and stress-/strain-dependent plastoviscoelastic rheology. However, this model could not resolve the fault localization. It reproduced surface uplift and subsidence under specific conditions irrelevant to our study (e.g., fixed magma chamber geometry). Thus none of the existing models really resolves the major problems as border fault formation and evolution and caldera collapse.

Calderas are commonly circular or ellipsoidal in shape, even in areas of strong regional extension where the major (tectonic) normal faults are linear. Well-known examples are represented by the Valles and

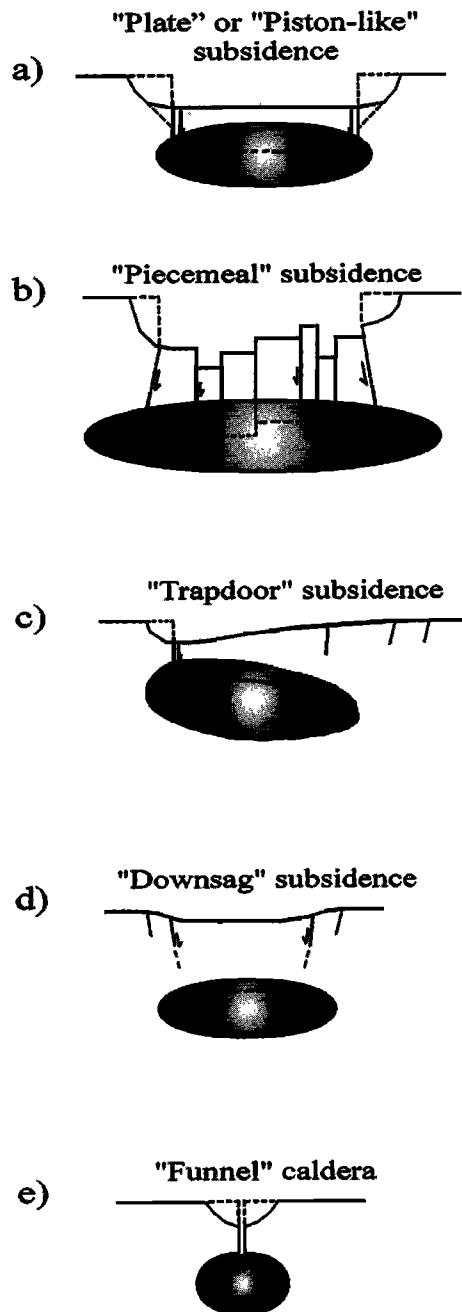


Figure 1. Five scenarios for caldera subsidence, adapted from *Lipman* [1997] and T. Druitt, (personal communication, 1998). The shapes and sizes of the magma chambers vary from one case to the other, indicating probable strong interplays between caldera subsidence style and reservoir geometry.

Questa calderas, located along the Rio Grande rift, and other nearly circular calderas are described by *Ofstedahl* [1978] within the Permian Oslo rift, in Norway. In some cases, the formation of a new small caldera embedded within an older large caldera can occur several million years after the major collapse, as at Rodalquilar-Lomilla in southeastern Spain [*Rytuba et al.*, 1990] and Platoro-Summitville in Colorado [*Lipman*, 1984]. Although the inner "nested" caldera may be geometrically similar to the outer one (nearly circular or elongate), this cannot be treated as a general rule; some calderas are highly asymmetric or exhibit an asymmetric dynamic behavior, as at the Toba caldera complex in Sumatra [*Chesner and Rose*, 1991].

Pyroclastic eruptions produce voluminous and thick ash flow tuffs that originate from shallow silicic intrusions. An idea of the quantities involved is given by the Bishop Tuff of the Long Valley caldera, which represents about 500 km³ of ejected products [*Bailey et al.*, 1976], by the deposits within the Julietta caldera, Russia, that are more than 1000 m thick [*Strujkov et al.*, 1996], and by the intracaldera tuffs at La Primavera, Mexico [*Mahood*, 1980]. The succession of volcanic events leading to the presence of thick intracaldera deposits is still not completely understood; although caldera collapse is commonly associated with the major eruption, recurrent caldera collapse and/or recurrent surface deformation have been also deduced for a number of ash flow calderas such as Santorini, Greece [*Druitt and Francaviglia*, 1992], and the Phlegraean Fields, Italy [*Bianchi et al.*, 1987].

Detailed hydrological and geothermal studies of the hydrothermal systems in ash flow calderas have focused on the flow paths of hydrothermal fluids [e.g., *Elder*, 1981; *Sorey et al.*, 1991; *McConnel et al.*, 1997]. None deal with the "large-scale" processes that, in our definition, include the caldera, the magma chamber, and their embeddings and involve large time spans; existing studies on active calderas such as Long Valley, Yellowstone, Taupo, or the Phlegraean Fields only yield information on the short-duration behavior. Fortunately, thermo-mechanical models can be constrained using petrophysical data available from abundant field and drilling studies.

In this paper, we investigate a number of the unresolved problems including the formation and deep geometry of the caldera faults, the thermal regime at depth, and the relationships between the magmatic system and the surface features of ash flow calderas. Our analysis is restricted to the effects of the reservoir geometry, the surface deposition, and the regional stress regime, all of which can affect the style of caldera collapse [*Lipman*, 1997]. Our study of thermal and mechanical processes within calderas, has incorporated experimentally constrained brittle-ductile-elastic rheological laws and laboratory measurements of thermal conductivities and densities, as well as the changes in these properties during caldera evolution. The first part of

the work is devoted to the steady state heat transfer (reflection and refraction) mechanisms related to the thermal conductivity contrasts within caldera settings. The second part deals with the physical mechanisms that lead to faulting and control the fault geometry, localization, and associated pressure/stress field and transient thermal effects. Finally, we present and discuss a coupled twofold thermomechanical model in which the heat diffusion and advection from the magma chamber affect the rheology of the caldera-related rocks, resulting in changes to the geometry of the fracture zones.

2. Physical Properties of Ash Flow Caldera Rocks

2.1. Intracaldera Units

Recent compilations of thermal conductivity data since the preliminary measurements by *Smith* [1960] show that the ash flow tuffs have high but quite variable porosity: porosity of the ash flow tuffs in the Guayabo caldera, Costa Rica, appears to range between 3 and 22% [*Hallinan and Brown*, 1995]; porosity values as high as 30% are reported for the intracaldera fill sequence of the Valles caldera [*Goff and Gardner*, 1994]; and the Neapolitan Yellow Tuffs of the Phlegraean Fields caldera have porosities reaching 50% [*Ascolese et al.*, 1993]. The conductivity-porosity histogram shown in Figure 2a (adapted from *Clauer and Huenges* [1995]) demonstrates that the high-porosity volcanic rocks (with a mean thermal conductivity k of 1.9 W m⁻¹ K⁻¹) are about 1.5-2.0 times less conductive than the other rocks, and Figure 2b shows that "tuff(ites)" belong to the family of volcanic rocks with the lowest possible thermal conductivity. A series of measurements in the ash flow tuffs of the Long Valley caldera, including the Bishop Tuff, gives k ranges from 0.8 to 2.2 W m⁻¹ K⁻¹ for the samples coming from shallow wells and a mean value of about 2.2 W m⁻¹ K⁻¹ for the Bishop Tuff [*Sorey et al.*, 1991]. The k values for shallow lying tuffs in the Phlegraean Fields are lower, between 0.40 and 0.85 W m⁻¹ K⁻¹, depending on the water content [*Corrado et al.*, 1998]. It must be noted that the surrounding rocks have rather high k compared to that of the ash flow tuffs; for example, Paleozoic metasediments of the Long Valley caldera and the adjacent granites are characterized by values of 4.2 and 2.8-3.3 W m⁻¹ K⁻¹, respectively. In other words, the ash flow tuffs are at least 1.3 times less conductive than the surrounding rocks, and this conductivity contrast can easily jump to more than 3.

The high porosity of the ash flow tuffs measured in the Taupo volcanic zone [*Cole et al.*, 1998] increases the density contrast between the intracaldera units and the embedding rocks. Ignimbrites, with density ranges between 900 and 2400 kg m⁻³, are basically less dense than other lavas. For example, the ignimbrite density in the Taupo volcanic zone is between 1300 and

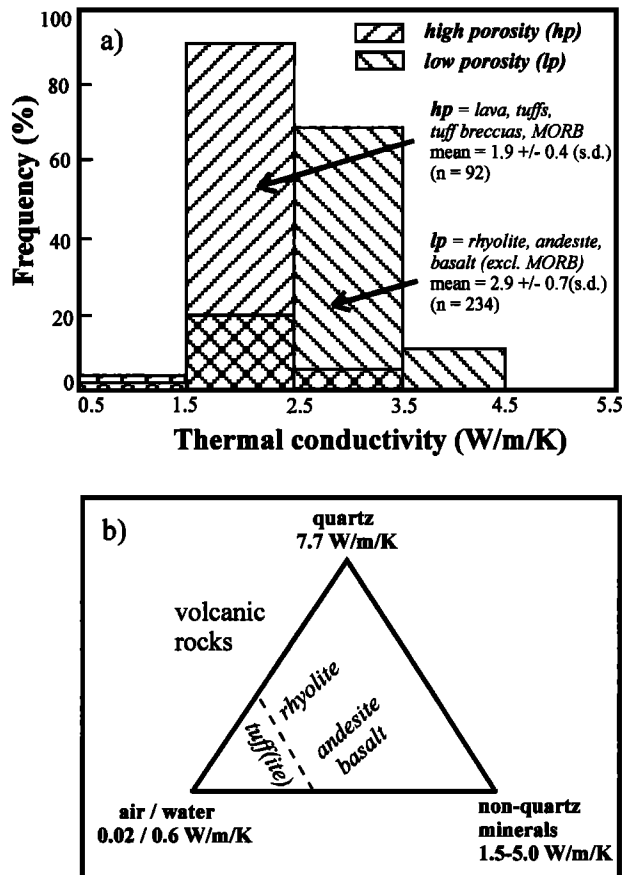


Figure 2. (a) Thermal conductivities of rocks present in ash flow caldera settings [from *Clauser and Huenges, 1995*]. (b) Quartz-rich rocks present in border faults of calderas are conductive material whereas tuff(ite)s are poorly conductive material. The effects of porosity (a) and pressure are discussed in the text.

2300 kg m⁻³; for the caldera fill sequences with ≈ 15% porosity at Valles caldera it is around 2200 kg m⁻³; for the Guayabo caldera, Costa Rica, it is between 900 and 2400 kg m⁻³ [*Hallman and Brown, 1995*]. From gravity modeling of the Los Azufres caldera, Mexico, *Campo-Enriquez and Garduño-Monroy [1995]* suggested a depth-averaged density contrast of -300 kg m⁻³ between the caldera infill and embedding rocks.

2.2. Fractured Rocks

Ring faults and fractures are locally filled with quartz rich rocks that, as suggested in Figure 2b [*Clauser and Huenges, 1995*], are probably more conductive than the other rocks. This is supported by recent heat flow studies [*Guillou-Frottier et al., 1996*] that suggest high k values for quartzites (around 5-6 W m⁻¹ K⁻¹, i.e., 2 times higher than for the crustal background and 4 times higher than for the intracaldera ash flow units. It is obvious that such a large lateral conductivity contrast between the caldera fill sequences and the caldera borders can modify steady state heat transfer patterns. Thus, if the width of the border faults essentially in-

creases with depth as suggested by *Rytuba [1994]*, we could expect the high-conductivity ring faults bordering the intracaldera ash flow tuffs to have a significant thermal effect, “channelizing” part of the lateral heat flow. It must be noted, however, that quartz-rich rocks become less conductive with increasing temperature, whereas the ash flow units are assumed to become less porous (and less insulating) with increasing depth. The combination of these two effects should result in depth-dependent conductivity contrasts between the ash flow tuffs and caldera faults. The effects of high- and low-conductivity rocks embedded within rocks of “normal” conductivity have still to be investigated. In the present study we merely take a first step forward by considering a simplified heat transfer model as presented in section 3.2.

3. Caldera “Snapping” and Heat Refraction: Analytical Assessment

In this section we make several simplified analytical estimations for the conditions of caldera subsidence and the thermal effects of the laterally varying thermal properties. In the later sections, based on the results of these estimations, we develop pure numerical models, free of the restricting assumptions imposed by the analytical approach.

3.1. Static Conditions of Caldera Snapping

Investigation of the thermomechanical behavior of ash flow calderas requires some simple initial idea of the conditions of their formation, such as location of the caldera with respect to the magma chamber, size and depth of the chamber, thickness of the deposits (which plays a double role as a surface load and as a thermal insulator), and critical overpressure in the magma chamber. Without at least an approximate knowledge of these parameters we may have difficulties in setting up the thermal and mechanical problem for numerical modeling.

A very simple mathematical formulation can be used to explain the formation and location of the ring faults. As was recently shown on the basis of analysis of bending and segmentation of the oceanic lithosphere at the spreading centers [*Buck, 1997*], a localized faulting or snapping (prior to distributed “crunching”) of a bent thin plastoelastic layer occurs when the maximum value of the local elastic bending moment exceeds the respective value of the plastic moment. *Buck [1997]* has shown that this condition is valid for layers thinner than 10 km. For our case, this implies that bending of the chamber roof (thickness of 2-3 km) should mostly result in localized faulting (and not in crunching) at the places of highest flexure and justifies our analytical model of roof bending and snapping (Figure 3) described in Appendix A. As predicted by our model, the maximum flexural stress σ inside the caldera roof is reached at the borders of its upper surface ($x = 0$); here it be-

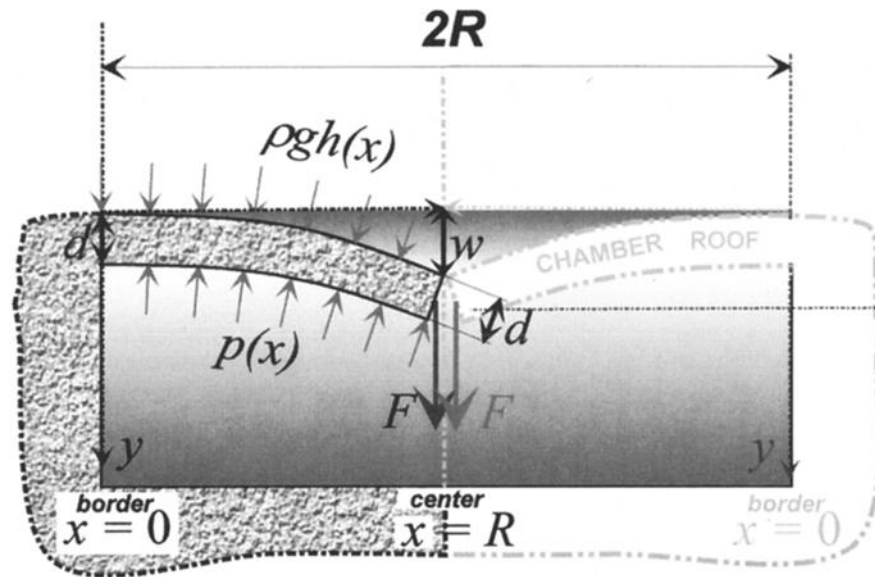


Figure 3. Diagram of the caldera roof snapping scenario; d is the roof thickness, R is the caldera radius, h is the thickness of the deposits, P is the overpressure, and F is the cutting edge force applied at the caldera center ($x = R$) (see text for definitions).

comes equal (see equation (A12)) to $3P(R/d)^2$, where P is the normal load applied to the cover (equal to the sum of the chamber pressure, weight of the deposits, ρgh (Table 1) and the other possible border forces), R is the radius of caldera, and d is the thickness of the strong part of the cover. The roof can break only if σ is greater than the local brittle rock strength σ_v , which is as little as 10 or 20 MPa at the surface and 2-3 times higher at the brittle-ductile interface with the magma chamber.

As follows from the relation for σ and from equation (A9) in Appendix A for the edge cutting force $F_c = \sigma d^2/6R$, the larger the caldera, the smaller the force or load needed to break it at the borders. For example, assuming $d = 2.5$ km, a thickness of at least 3 km of ash flow deposits will be needed to provoke border faulting and the collapse of a small caldera with $R = d$ ($2R/d = 2$). A larger caldera with $R = 10$ km ($2R/d = 8$) will collapse under a much (16 times) lower load, corresponding to only a 20-m-thick surface deposit layer or to overpressures in the magma chamber of only few megapascals. The same argument is valid for the critical edge force, which is several times higher for a small caldera ($2R/d = 2$) than for a large one ($2R/d > 6$). Thus only a 10 m thickness of surface deposits, or ~ 1 MPa of the subsurface overpressure, will be sufficient to break the roof of a magma chamber with $(2R/d) = 10$, as against values 25 times greater for a caldera with $(2R/d) = 2$ and 100 times greater for a caldera with $(2R/d) = 1$.

In general, one needs a higher bending stress to break the magma chamber roof from below than from above because the brittle rock strength σ_γ increases with depth z (or pressure) by $\approx 0.6 \rho g(z + h)$ for compression and $\approx 0.3 \rho g(z + h)$ for extension; a σ_γ of ~ 10 - 20

MPa for granite-like rocks at the upper surface of the chamber roof would be from 20-30 to 40-60 MPa at the interface with the magma chamber. Consequently, one can assume that the rupture is more likely to be initiated at the surface, either, and most probably, (1) at the initial stages of upward roof and local extension due to overpressure in the chamber before the eruption or (2) at the stage of downward roof flexure under the load of the erupted deposits and due to the underpressure in the partly emptied magma chamber. In the latter case, the rupture may start both at the top and at the bottom of the cover because even though the rock strength increases with depth, the extended lower part of the chamber roof may appear weaker than the compressed upper part due to the asymmetry in response to compression and extension.

Unfortunately, the thin-plate approximation does not allow one to account for stress depth distributions associated with the real geometry and mechanical properties of the system. Moreover, the assumption of a rigid flexible cover would not work for very shallow or very "hot" calderas where the cover may no longer be rigid. As will be shown in later two-dimensional (2-D) modeling sections, faults do indeed tend to initialize at the borders but may propagate in directions opposite to what is expected in the elastic model. This is due mainly to the additional strain localizations around the curved corners of the magma chamber and to depth-dependent inelastic rheological properties.

In cases where $R > \lambda$ (with $\lambda \simeq (4-5) d$ being the flexural wavelength [*Timoshenko and Woinowsky-Krieger*, 1959]), the second derivative of the deflection, w'' , will have more than one local extreme. Consequently, the roof of the magma chamber may also be broken in the intermediate zones between the center and the borders

Table 1. Definition of Variables

Variable	Values and Units	Definition	Comments
a	n.d.	inner caldera radius	analytical thermal model
a_m	n.d.	Fourier coefficient	analytical thermal model
A	$\text{Pa}^{-n} \text{ s}^{-1}$	material constant	power law
b	n.d.	outer caldera radius	analytical thermal model
b_m	n.d.	Fourier coefficient	analytical thermal model
c_m	n.d.	Fourier coefficient	analytical thermal model
d	km	caldera roof thickness	
D	N m	flexural rigidity	
E	$8 \times 10^{10} \text{ N m}^{-2}$	Young's modulus	
fw	n.d.	fault width	$fw = b - a$
F	N m^{-1}	force	per unit width
g	9.8 m s^{-2}	acceleration due to gravity	
h	m, km	thickness of deposits	ignimbrites
h_r	10 km	decay scale of heat production	upper crust
H	km	chamber thickness	
H^*	kJ mol^{-1}	activation enthalpy	power law
H_s	$9.5 \times 10^{-10} \text{ W kg}^{-1}$	surface heat production rate	upper crust
$H_{c2} C_{c2}^{-1}$	$1.7 \times 10^{-13} \text{ K s}^{-1}$	radiogenic heat	lower crust
k	$\text{W m}^{-1} \text{ K}^{-1}$	thermal conductivity	
k_i	n.d.	thermal conductivity	ignimbrites
k_f	n.d.	thermal conductivity	fault
k_1	n.d.	thermal conductivity	host rocks
k_{c1}	$2.5 \text{ W m}^{-1} \text{ K}^{-1}$	thermal conductivity	upper crust
k_{c2}	$2.0 \text{ W m}^{-1} \text{ K}^{-1}$	thermal conductivity	lower crust
k_m	$3.5 \text{ W m}^{-1} \text{ K}^{-1}$	thermal conductivity	mantle
K_d	$\text{m}^2 \text{ s}^{-1}$	coefficient of diffusion	mass diffusivity
L	250 km	thermal thickness of the lithosphere	
m	n.d.	index of Fourier series	
M	N	flexural moment	per unit length
n	3 to 5	stress exponent	power law
p	Pa, MPa	pressure	
P	Pa	normal load	or overpressure
q_m	n.d.	wavenumber	analytical thermal model
r_{xy}	km, m	roof curvature	
r_k	1.5 to 10	conductivity ratio	$r_k = k_f/k_i$
R	km, m	caldera radius	
R^*	$8.314 \text{ J mol}^{-1} \text{ K}^{-1}$	gas constant	power law
t	s	time	
t_a	Ma	thermal age	less than geological age
T	$^{\circ}\text{C}$, K	temperature	depending on usage
T_e	m, km	effective elastic thickness	instant integrated strength
T_m	1330°C	T at depth L	
w	m, km	roof deflection	
x	n.d., m, or km	horizontal distance	analytical models
y	m, km	depth	analytical mechanical model
z	0 to 1 (n.d.)	depth	analytical thermal model
α_m	n.d.	Fourier coefficient	analytical thermal model
β_m	n.d.	Fourier coefficient	analytical thermal model
γ_m	n.d.	Fourier coefficient	analytical thermal model
ε	n.d.	strain	
$\dot{\varepsilon}$	s^{-1}	average strain rate	

(see flexural equations (A1)-(A2)). Such configurations could give rise to the formation of the so-called nested calderas, even though this scenario is not necessarily unique.

The derivations of this section were made in the traditional way, i.e., without taking into account the thickness H of the magma chamber itself. For $d \ll H$ and $d < (4-5) R$ (typical thin-plate constraints), the thin-

plate approximation should be still valid for the chamber cover. However, if the thickness of the chamber approaches the thickness of its cover, the flexural behavior of the latter will be much more complex since it may become coupled with the deformation of the whole magmatic system. Such coupling may increase the integrated strength of the "roof-magma chamber" system and result in larger deformation wavelengths. Another

Table 1. (continued)

Variable	Values and Units	Definition	Comments
κ	$\text{m}^2 \text{s}^{-1}$	thermal diffusivity	$\kappa = k/\rho C_p$
κ_{c1}	$8.3 \times 10^{-7} \text{ m}^2 \text{ s}^{-1}$	thermal diffusivity	upper crust
κ_{c2}	$6.7 \times 10^{-7} \text{ m}^2 \text{ s}^{-1}$	thermal diffusivity	lower crust
κ_m	$8.75 \times 10^{-7} \text{ m}^2 \text{ s}^{-1}$	thermal diffusivity	mantle
μ	Pa s	effective viscosity	10^{19} to 10^{27} Pa s
ν	0.25	Poisson's ratio	
ρ_{c1}	2650 kg m^{-3}	density	upper crust
ρ_{c2}	2900 kg m^{-3}	density	lower crust
ρC_p	$\text{J m}^{-3} \text{ K}^{-1}$	density \times specific heat	
$\sigma_{xx}, \sigma_{xy}, \sigma_{yy}$	Pa, MPa	stress components	

Here n.d. stands for dimensionless units

shortcoming of the simplified model is related to its inability to reproduce fault geometries and to account for interactions between the thermal and mechanical behaviors.

3.2. Steady State Heat Refraction

3.2.1. Analytical model. Previous studies have considered the effects of heat reflection and refraction for particular cases [Lee and Henyey, 1974; Stephenson *et al.*, 1989; Lobkovsky and Kerchman, 1992], but little has been done in relation to heat refraction at depth, which is quite different from that at the surface. In this study, we focused on temperature distribution and horizontal and vertical temperature gradients and heat fluxes. In order to obtain easily interpretable results we chose a simplified geometry that includes a rectangular caldera surrounded by thin vertical border faults and

placed in a semi-infinite crustal layer (Figure 4). This model is based on the solution of thermal diffusion equations (see Appendix B) and has four major variable parameters: two geometric parameters (caldera and fault widths normalized to the vertical size of the system) and two thermal parameters (conductivity of intracaldera units, or ignimbrites, and conductivity of fault infill, normalized to that of the crust). One could also use a cylindrical or elliptical shape [Lee and Henyey, 1974] for the system geometry, but it has been already shown that the Cartesian model provides a lower limit on the heat transfer anomalies because it tends to give systematically smoother anomalies than the cylindrical or elliptical model [see Guillou-Frottier *et al.*, 1996, Figure 4]. In sections 3.2.2-3.2.3 we concentrate on the effects of varying thermal conductivities and fault widths on the deep heat transfer.

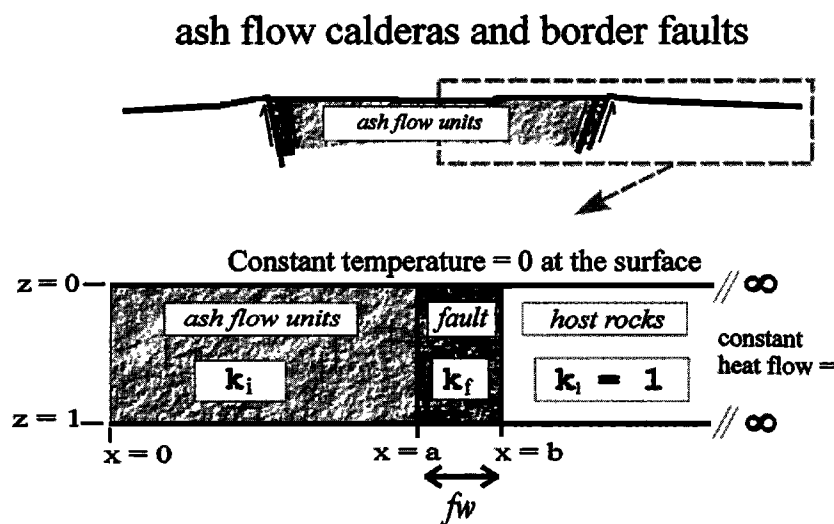


Figure 4. Diagram of the thermal model used to investigate the heat refraction effects within caldera settings. Ignimbrites (insulating ash flow units) fill the internal part of the caldera, and conductive quartz-rich rocks are present in the border faults. Boundary conditions are detailed in the text and in Appendix B. Caldera diameter is assumed to be large enough to maintain a constant undisturbed surface heat flow at the center $x = 0$. This simple geometry has been chosen to evaluate the depth dependence of heat transfer mechanisms.

Previous studies devoted to heat refraction at the surface ($z = 0$) have shown that thermal gradients measured over conductors with small aspect ratios do not exhibit important variations, whereas the surface heat flow may vary significantly [Guillou-Frottier *et al.*, 1996]. This phenomenon can be easily explained as a result of the constant temperature condition at the surface, enforcing smooth variations of the temperature gradients below the surface. The analytical solutions given in Appendix B allow us to investigate the deep steady state heat transfer mechanisms; however, it should be noted that one physically valid condition for large calderas (an undisturbed and constant heat flow value at the center of the caldera) has been chosen for this simplified model. Tests of other conditions at the center of the caldera did not result in the same thermal field, but they were also less representative of an “insulating embedded caldera.”

3.2.2. A deep-seated thermal anomaly. Figures 5, 6, and 7 show how lateral thermal conductivity variations disturb the isotherms and heat transfer at depth. Even though this model is simplified (mainly Cartesian geometry, steady state regime, “dry” conditions, large caldera hypothesis), it appears to be largely sufficient to demonstrate a number of quite unexpected thermal effects.

Figure 5 is divided into two parts, the center of the caldera being located at $x = 4$ and the border faults at $x = 1$ (Figure 5, left) and $x = 7$ (Figure 5, right). The dimensionless thermal conductivity of the ignimbrites is the same in both cases ($k_i = 0.3$). In the case in Figure 5(left), the fault is represented by a vertical interface of zero width ($fw = 0$) and the ignimbrites contact directly with the host rocks. For the case in Figure 5(right), the fault is wide ($fw = 0.1$) with a conductivity ratio of $r_k = 7$ ($k_f = 2.1$). Surface anomalies of the vertical temperature gradients (G_0) and heat fluxes (F_0) are also shown at the bottom of Figure 5. Temperature (T) and vertical gradient (G) are continuous through any horizontal plane, whereas the vertical heat flow (F) has discontinuities on the sides of the vertical interfaces.

In Figure 5(left) ($fw = 0$), low heat flow values are obtained near the inner side (to the right) of the discontinuity because the temperature gradient decreases from the center ($x = 4$ in Figure 5) to the edge ($x = 1$) of the insulating part of the model. On the outer side of the discontinuity, the better conducting rocks promote a higher heat flow. The vertical heat flow anomaly is located in the vicinity of the discontinuity, and the heat flow almost recovers its undisturbed state, in the host rocks in Figure 5(left).

In Figure 5(right) ($fw = 0.1$, same k_i of 0.3, and $r_k = 7$), the bottom plot shows that the surface vertical heat flow jumps over the fault, while the surface temperature gradient stays the same as for the previous case (see complementary plot in Figure 5(left)). In this case, the vertical variation of the temperature gradient G within and around the fault at depth is quite irreg-

ular; one can see a distortion of the iso- G lines (star), showing that the excessive heat is more easily transferred from the ignimbrites to the host rocks when a contrasting conductive inclusion (fault) is present. This is also outlined by the higher values of the horizontal heat flow (f) near the bottom part of the fault.

3.2.3. Fault widths and conductivity ratios. The effect of the lateral heat transfer near the bottom of the fault is shown at a larger scale in Figure 6, where the fault width has been varied from 0 to 0.06, for a constant value of k_i ($= 0.4$). Because the temperature is fixed at the upper surface, there is no strong distortion of temperature gradient near the upper surface. At depth, however, the presence of the conductive fault ($k_f = 2.0$) increases the temperature gradients around and within it. In the case of a “thick” fault (Figure 6 (bottom)), one notes at the outer edge (right side) at depth, an increase followed by a decrease in the vertical temperature gradient G . This phenomenon is due to the adjustment of the thermal field to the changes in fault width and conductivity values. For a thin fault this local maximum of temperature gradient would be observed only for rather large conductivity contrasts, exceeding any reasonable values. When a distorted iso- G line crosses the fault, a vertical heat flow anomaly appears at its outer side. As can be observed from Figure 6, the wider the fault, the stronger the anomaly. However, the relative effects of variations in r_k , k_i , and k_f are not so obvious and thus have to be investigated.

With large calderas, as has been shown, the thermal field is disturbed over distances that are much shorter than the width of the caldera. Consequently, the high conductive fault can be considered as a finite width vertical layer sandwiched between two different media composed of low conductive ignimbrites (inner or caldera side) and the host rocks (outer side). The medium with a smaller conductivity difference (the host rock, by definition, $k_i < k_1 < k_f$) will disturb the thermal field in the vicinity of the fault to a less extent than the medium with the higher conductivity contrast (intra-caldera units). Consequently, since in nature the conductivity ratio r_k can be hardly higher than 10, and k_f/k_1 is < 2 , one can expect that the effect of variation in r_k is controlled primarily by the ignimbrite conductivity k_i and not very much by the values of k_f .

Figure 7 shows the results of several tests where G is plotted versus horizontal distance for fixed depths. In Figure 7(top), r_k is increased by changing both k_i and k_f . The thermal anomaly is observed at the outer side of the fault when G values are greater, for example, at depth $z = 0.95$ than at depth $z = 0.99$; we have obtained similar signatures for a fixed value of $r_k = 3$ and variable k_i and k_f . Figure 7(middle) shows three cases where k_i is fixed at 0.4, while r_k increases from 3 to 6. The experiments in Figure 7(top) and Figure 7(middle) show that that a significant thermal anomaly is present (marked by star) when the ignimbrites are sufficiently insulating, regardless of the value of k_f . Figure 7(bot-

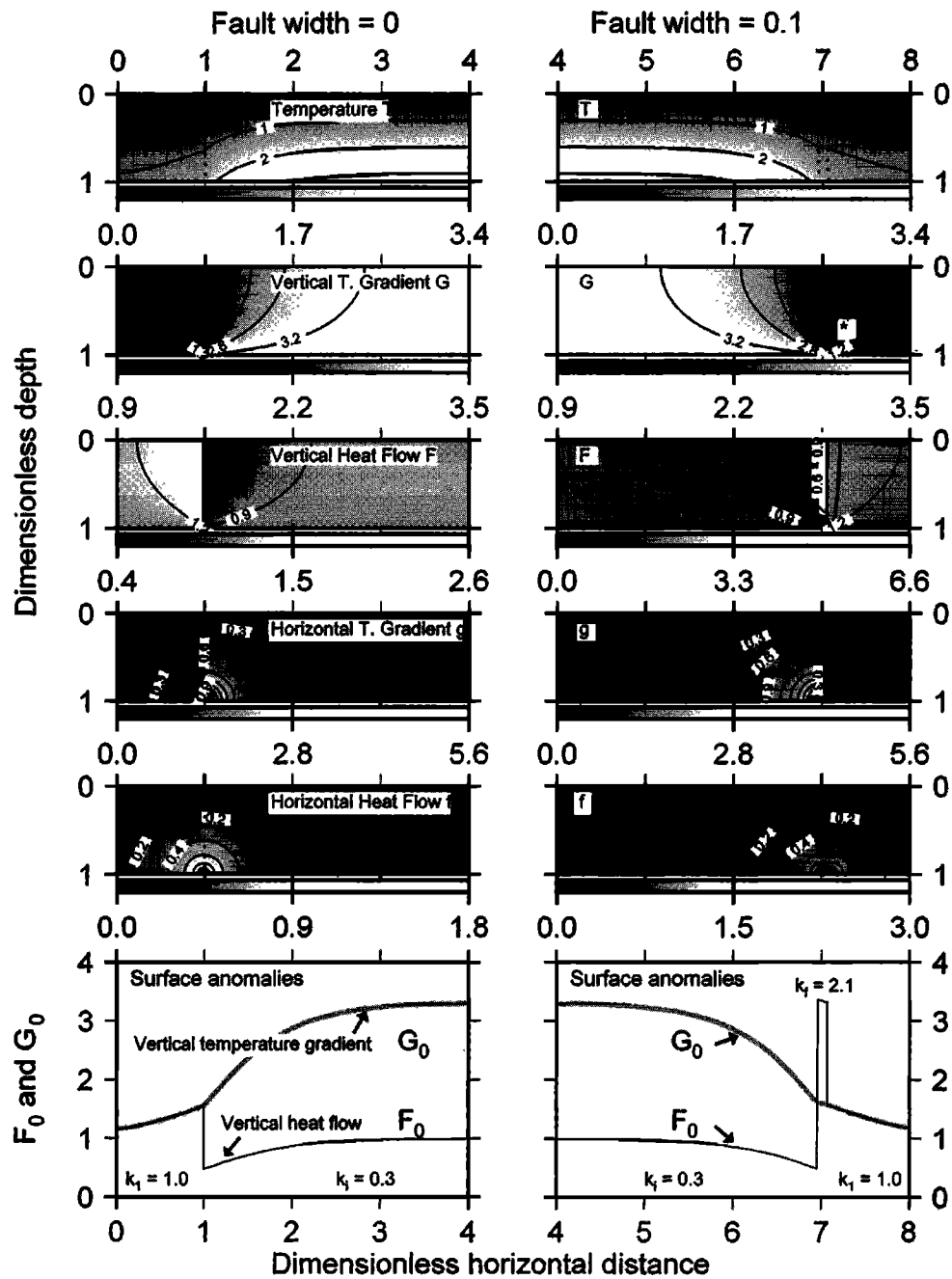


Figure 5. Thermal field within and around the caldera for two cases. On the left, results for a fault of no width; on the right, results for a fault with width $fw = 0.1$ to emphasize the thermal anomaly (star). However, the conductivity ratio $r_k = 7$ ($k_f = 2.1$ and $k_i = 0.3$) stays within the reasonable range of values. Temperatures T and the other values are dimensionless (see text), while the undisturbed heat flow value equals 1. (top) Isotherms uplifted by the insulating effect of the ignimbrites. Horizontal heat flow f is continuous through the vertical discontinuities, contrarily to the horizontal temperature gradient g . For no width, the vertical temperature gradient G near the fault shows a smooth variation with increasing depth, in contrast to the case on the right. Sharp vertical heat flow variations (F) are observed close to the discontinuity. For large width, variations of G and F with depth show that the fault width accounts for the lateral heat transfer from the ignimbrites to the host rocks. (bottom) The surface ($z = 0$) anomalies G_0 and F_0 , with no surprising effect (heat flow shows a peak over the conducting fault). Indeed, the fixed temperature condition at the surface implies that the anomaly must be deep seated.

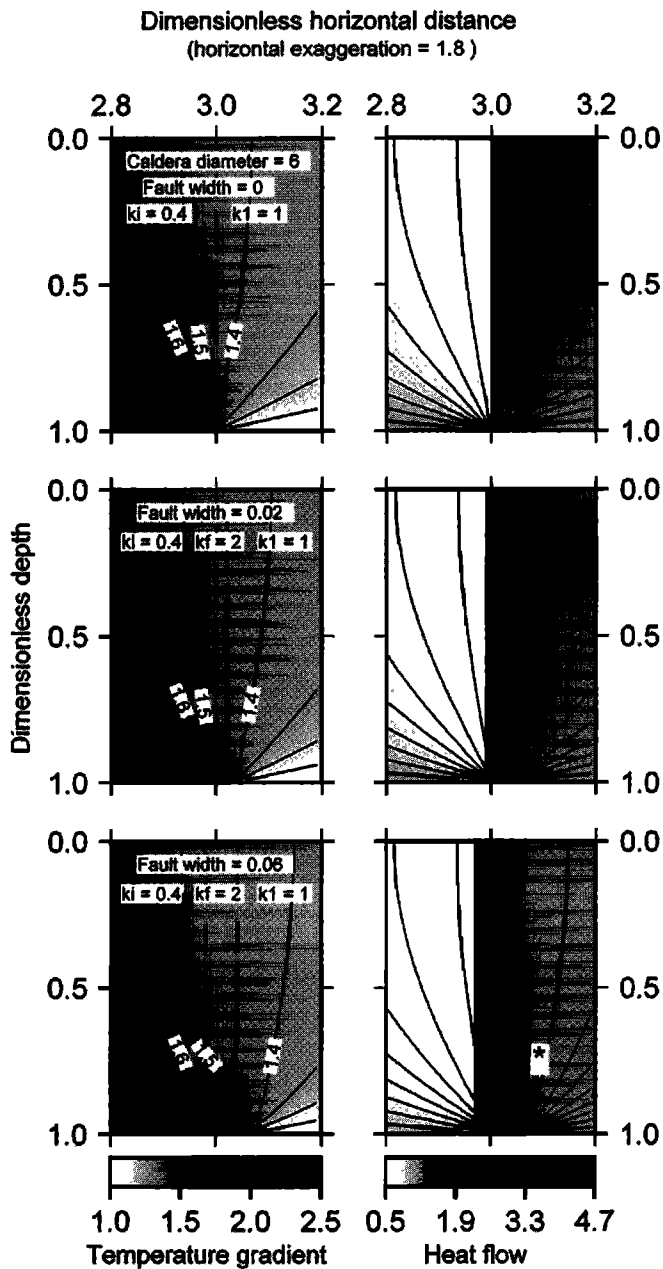


Figure 6. Details of the vertical temperature gradient G and heat flow F near the conductive fault, for three fault widths ($fw = 0, 0.02,$ and 0.06). The positive anomaly (star) appears on the outer side of the fault (within the embedding rocks) and for the largest fault widths. Lateral heat transfers are discussed in the text.

tom) demonstrates the effect of different fault widths at fixed conductivity values, and the geometric effect is clearly seen in the development of the anomaly. For a wide conductive fault, temperature gradients remain rather high at the outer side of the fault (see also Figure 6), leading to a more disturbed thermal field outside of the caldera.

Obviously, the obtained results depend on the chosen boundary conditions that are detailed in Appendix B. Among these, the finite width of the caldera, leading to no lateral heat conduction at the center, allows the ther-

mal anomaly to develop. Tests where a conductive fault was embedded within two semi-infinite insulating media (and hence with no symmetry in the solution) did not yield thermal anomalies at the outer sides of the fault. Heat excess from both sides of the fault was transmitted inside the fault. However, this problem does not correspond to our study where unusual rocks are represented by intracaldera units and not by the fault.

4. Coupled Thermomechanical Numerical Model

4.1. Numerical Approach

To investigate the coupled thermomechanical evolution of the calderas, we adopted a numerical approach that allows for brittle and nonlinear viscous (i.e., ductile) rheology and complex geometrical structures. This approach is based on the PARAVOZ code, the kernel of which was derived by A.N.B. Poliakov and Y. Podladchikov [Poliakov *et al.*, 1993a, b] from the Fast Lagrangian Analysis of Continua algorithm (FLAC[®]) originally developed by P. Cundall [Cundall and Board, 1988; Cundall, 1989]. Like FLAC[®], PARAVOZ is a large strain and fully explicit time-marching numerical algorithm based on the Lagrangian moving mesh method. The latter allows for large-strain solution of Newton's full dynamic equation of motion holding a locally symmetric small-strain formulation generally used in continuum mechanics:

$$\rho \partial v_i / \partial t - \partial \sigma_{ij} / \partial x_j - \rho g_i = 0, \quad (1)$$

where $\partial v_i / \partial t$ is acceleration, g is the acceleration due to gravity, and ρ is the density. In its generic form, Newton's equation of motion inherently implies the other Newton laws and the conservation laws (momentum and energy). Equation (1) is derived from this equation of motion, under the assumption of continuum finite deformation of an incompressible body based on local observance of the linear momentum principle and using the divergence theorem of multivariable calculus. Hence equation (1) corresponds to small-strain formulation but can be used for globally large-strain problems if solved in local coordinates by updating these coordinates at each time step in large-strain mode. In the Lagrangian method the incremental displacements are added to the coordinates, allowing the mesh to move and deform with the material. Unlike common implicit finite element methods (FEM), FLAC[®] methods do not need to form a global stiffness matrix, which makes the coordinate updates very simple: at each time step the new positions of the mesh grid nodes are calculated from the current velocity field using an explicit procedure (two-stage Runge-Kutta). For example, the local area rotation at large strain is taken into account by adjusting the local stress tensor components $\sigma_{ij} = \sigma_{ij} + (\omega_{ik} \sigma_{kj} - \sigma_{ik} \omega_{kj})$, where finite rotation ω is computed as $\omega_{ij} = \frac{1}{2}(\partial v_i / \partial x_j - \partial v_j / \partial x_i)$ [Cundall, 1989]. This pa-

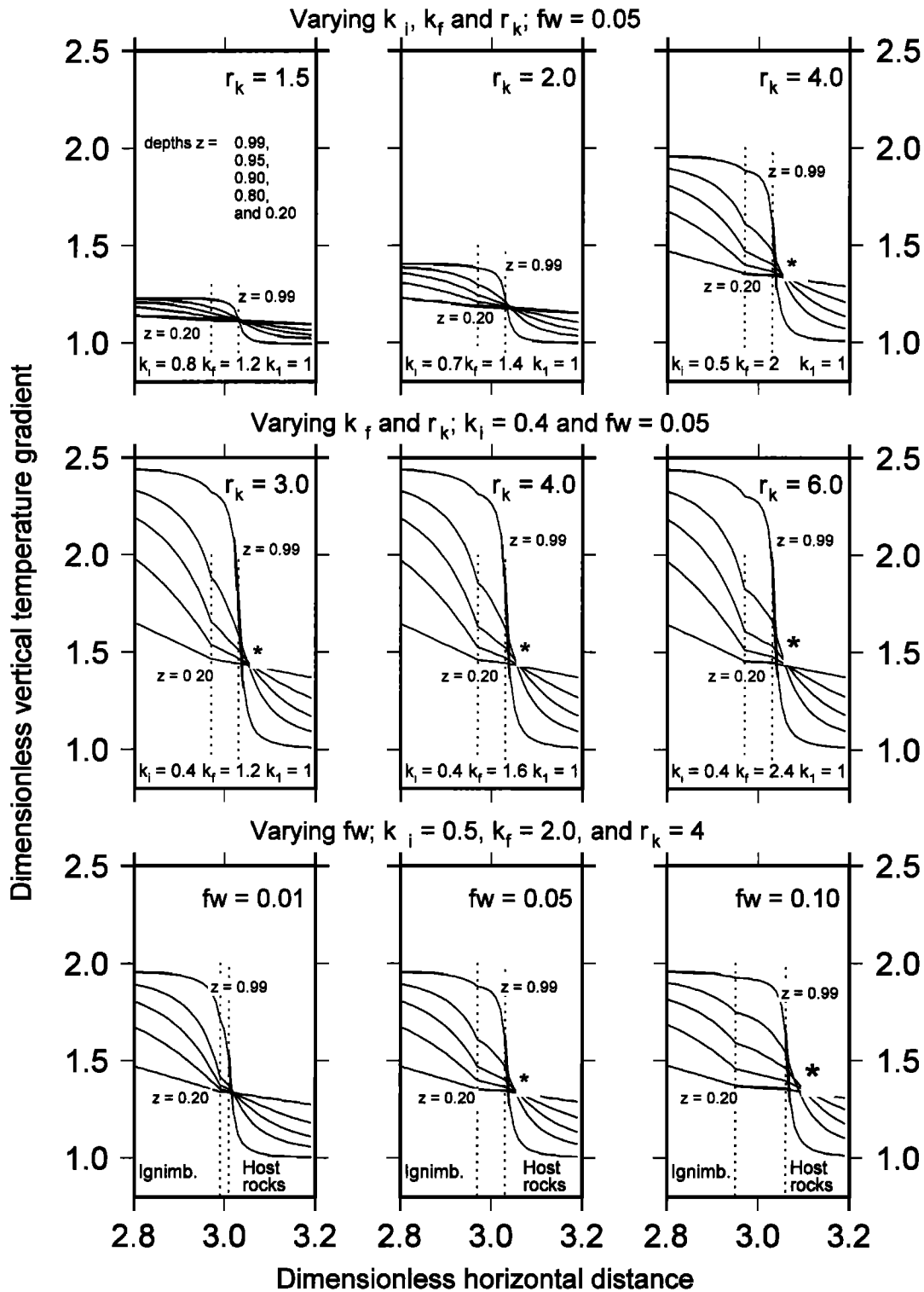


Figure 7. Depth variation of horizontal cross sections (fixed values for z) of the temperature gradient in and around the fault; r_k is varied together with k_i and k_f (top); r_k is varied while $k_i = 0.4$ is fixed (middle); and (bottom) fault width fw is varied for fixed values of r_k and k_i . The presence and the size of the star indicate the relative importance of the thermal anomaly.

per deals with locally plain-strain continuum mechanics problems and thus the assumption of locally symmetric strain/stress tensor in equation (1) holds.

Even for static problems, the use of dynamic equations of motion is an important advantage because it en-

sures that the numerical scheme is stable even when the modeled physical system is unstable, as is quite often the case with nonlinear materials such as crustal rocks and magma. The solutions to the equations of motion provide velocities at mesh points, which are used to cal-

culate element strains ε_{ij} . These strains are then used in constitutive relations to calculate element stresses σ_{ij} and equivalent forces ($\rho \partial v_i / \partial t$), which form the basic input for the next calculation cycle. For elastic and brittle [Byerlee, 1978] materials the constitutive relations have the form

$$\varepsilon_{ij} = C \sigma_{ij} + C_0 \quad (2)$$

with C, C_0 being material parameters. For ductile rheology the constitutive relations become

$$\dot{\varepsilon}_{ij} = B \sigma^{n-1} \sigma_{ij}, \quad (3)$$

where $\dot{\varepsilon}_{ij}$ is the strain rate, and $\sigma = (\frac{1}{2} \sigma_{ij} \sigma_{ij})^{1/2}$ is the effective stress (second invariant of the deviatoric stress tensor). The parameters n (the effective stress or power law exponent) and B (constitutive parameter) describe the properties of a specific material. For the dislocation creep, $B = A e^{-H^*/R^*T}$. The exponent n usually equals 3 to 5 and A (material constant) is depth- and temperature-dependent (Table 1 and Table 2); see also [Kohlstedt et al., 1995]. For brittle and elastic materials, C is usually only depth-dependent (though it may depend on strain and stress for some brittle materials). The plastic rheology used here is a cohesion-softening Mohr-Coulomb plasticity with friction angle 30° and cohesion decreasing from 20 MPa at zero strain to 0 at 0.01 strain. These parameters are supposed to reproduce the brittle properties of the subsurface rocks [Gerbault et al., 1998]. The values for the other material parameters are given in Tables 1 and 2.

The FLAC[®]-like algorithm used in PARAVOZ combines the advantages of the classical finite difference method (explicit time-marching solution of the algebraic equations making it possible to deal with ill-

behaved systems) with some advantageous features of the FEMs such as implicit matrix-oriented solution schemes and the possibility of using custom-shaped elements. To allow for the explicit solution of the governing equations, the FLAC[®] method employs a dynamic relaxation technique based on introducing artificial inertial masses in the dynamic system. Physical instabilities are thus treated in a natural way, i.e., through dissipation of the strain energy by converting it into kinetic energy. The adaptive remeshing technique [Poliakov et al., 1993a, b] enables one to resolve strain localizations leading to formation of the faults. Since some of the rheological parameters are temperature-dependent, equations (1) to (3) are coupled with the thermal transport equation:

$$\rho C_p \partial T / \partial t - \text{div}(\mathbf{k} \cdot \nabla T) + (\mathbf{v} \cdot \nabla) T = H_s, \quad (4)$$

where \mathbf{v} is the velocity tensor, C_p is the specific heat, \mathbf{k} is the thermal conductivity tensor, H_s is radiogenic heat production per unit volume (here we use the values adopted by Burov et al. [1993]; see Table 2). Technically, the temperature increment due to the diffusive and heat generation terms is calculated on each time step, whereas that due to the heat advection term is accounted for automatically by deforming the temperature field together with the displacement field. This splitting is possible because a very short automatically adoptive time step is used, chosen to satisfy the "frozen field" condition [Marti and Cundall, 1982]. This means that the time step is computed to be so short that information (stress, heat, etc.) cannot significantly propagate between the neighboring elements during a single step. The solver of the FLAC[®] method does not imply any inherent rheology assumptions, unlike most common finite element techniques based on the displace-

Table 2. Parameters of Dislocation Creep for Lithospheric Rocks and Minerals

Mineral/Rock	$A,$ $\text{Pa}^{-n} \text{ s}^{-1}$	$H^*,$ kJ mol^{-1}	n
Quartzite (dry)	5×10^{-12}	190	3
Diorite (dry)	5.01×10^{-15}	212	2.4
Diabase (dry)	6.31×10^{-20}	276	3.05
Olivine/dunite (dry) dislocation climb at $\sigma_1 - \sigma_3 < 200$ MPa	7×10^{-14}	520	3
Olivine Dorn's dislocation glide at $\sigma_1 - \sigma_3 \geq 200$ MPa			

$$\dot{\varepsilon} = \dot{\varepsilon}_0 \exp \left[\frac{-H^*(1 - (\sigma_1 - \sigma_3)/\sigma_0)^2}{R^*T} \right],$$

where $\dot{\varepsilon}_0 = 5.7 \times 10^{11} \text{ s}^{-1}$
 $\sigma_0 = 8.5 \times 10^3 \text{ MPa}$ and $H^* = 535 \text{ kJ mol}^{-1}$

These values correspond to the lower bounds on the rock strengths [Brace and Kohlstedt, 1980; Carter and Tsenn, 1987; Tsenn and Carter, 1987; Kirby and Kronenberg, 1987].

ment method and requiring formulation of new finite element types for each new rheology. Owing to this FLAC[®] feature, arbitrary nonlinear constitutive laws can be easily plugged into the numerical scheme without any additional subiterations and be treated in a valid physical way. The other advantage of the FLAC[®] method over most common techniques is that no large stiffness matrix assemblages are to be inverted during the computations. This allows for much better numerical resolution and larger displacements than can be usually afforded using a traditional FEM code. Thus, in our problem, one can simulate the formation of nonpredefined faults using a uniform high-resolution grid. This is different from most other techniques, which would require either specially predefined elements (e.g., slippery nodes) or local mesh prerefinements, both unacceptable in our case.

4.2. Mechanical Model Setup

We use a full 2-D Cartesian model with no axial symmetry, which is needed to reproduce asymmetric features in caldera and border fault geometry. In this study we chose a classical scenario with a central evacuation vent. Our thermomechanical model comprises a 50 km \times 20 km box with crustal rheology, which embeds a rectangular magma chamber of thickness H (5 to 10 km). The top of the chamber is placed at a depth d (2 to 5 km) below the surface (Figure 8). The diameter of the chamber is equal to $2R$ and has been varied between d and $25d$. The numerical grid consists of 16,000 to 256,000 quadrilateral elements of size 250 m \times 250 m to 72.5 m \times 72.5 m.

To prevent mesh-locking at large strains, each element is composed of two overlaid couples of constant-strain triangular subelements. The embedding rock is presented by two rheological layers: a 10-km-thick elastic-plastic (Mohr-Coulomb)-ductile upper crust layer with friction angle 30° , and a 10-km-thick elastic-plastic-

ductile lower crust layer with similar rheology but with higher density (Table 2). The effective (nonlinear) viscosity $\mu_{\text{eff}} = \sigma(2\varepsilon(\sigma, P, T))^{-1}$ of the layers is determined by the ductile creep law (Table 1) and is strongly temperature- (T), pressure-depth- (P), and strain rate (ε)-dependent. For the representative rheological parameters (Table 1) the viscosity changes by a factor of ± 10 above and below the depth corresponding to the mean value of 10^{20} Pa s. The elastic parameters are identical for both layers (Young's modulus $E = 0.8$ GPa and Poisson ratio $\nu = 0.25$). The magma chamber is filled with hot (and thus low viscosity) quartz-controlled (silicic) magma. Theoretically, at 800°C , the magma viscosity may be as low as 10^6 - 10^7 Pa s [Clemens, 1998; C.Jaupart, personal communication, 1998]. The characteristic times in the model are determined by the kinematic boundary conditions and by viscous response of the embedding crust. However, the characteristic times in the model are thus determined by the velocity boundary conditions and by the viscous response of the embedding crust. Associated deformation rates are of the order of 10^{-13} s $^{-1}$, which yields negligibly low magma stresses of 10^{-8} Pa. For this reason, there is no need to represent the entire viscosity range in the model, and any significant viscosity contrast (2-5 orders) between the magma chamber and the embedding rock would be sufficient to calculate deformation of the magma chamber [Chéry *et al.*, 1991]. We chose a value of 10^{16} Pa s which is 3 to 5 orders lower than the viscosity of the upper and lower crust (10^{19} to 10^{21} Pa s).

Largely to save CPU time, the magma convection was not modeled. To simulate thermal and mechanical conditions of the upper boundary layer present in the convecting magma chamber, the upper quarter of the magma chamber was not filled with hot magma but was "substituted" by constant overpressure of 10 MPa (most commonly inferred value [e.g., Chéry *et al.*, 1991]) where heat diffusion only occurs. Short timescale pres-

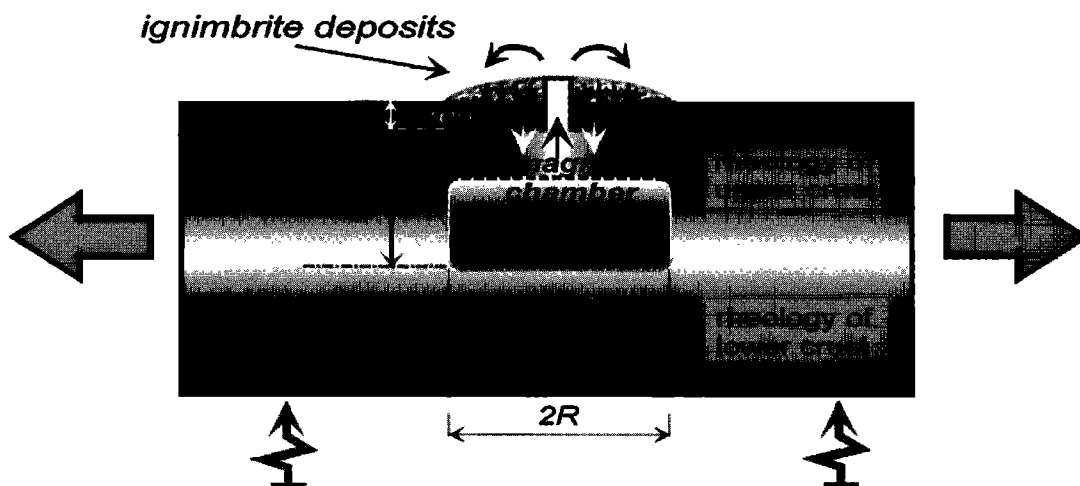


Figure 8. Setup for the mechanical numerical model. Properties of the materials are given in Tables 1 and 2.

sure variations, induced for example by magma-water interactions [Dobran and Papale, 1993], are not considered in our model. Because the upper part of the partly emptied reservoir is void of magma, this layer acts as a thermal insulator (thermal conductivity of the “empty” elements is replaced by that of the air). Direct heat radiation through a transparent gas layer and gas convection are not considered.

4.3. Boundary and Initial Conditions

The bottom condition is a pliable Winkler basement, which simulates the response of the underlying weak lower crust (for the geotherm and depth interval used, the viscosity of the lower crust is $\sim 10^{19}$ Pa s). The lateral boundary conditions are given in velocities. In the calculations, the amount of material that leaves through the evacuation vent is redistributed around on the surface. We used a diffusion mass transfer law on the surface to redistribute extruded and eroded matter [Avouac and Burov, 1996]. This law has a form $\partial h/\partial t = K_d \Delta h$, where K_d is a scale-dependent diffusion/erosion coefficient and h is the surface elevation. K_d was adjusted empirically to achieve timely redistribution of the extruded material. The choice of this, or any other, law is not principally important, but it is known that diffusion allows for more realistic deposit layering than, for example, flat deposition and automatically insures mass conservation for the extruded material. The volume of the extruded material is calculated from the imposed conditions on the overpressure in the magma chamber. For simplicity, the overpressure was kept constant in these experiments.

4.4. Numerical Experiments

The thickness d of the ignimbrite calderas does not significantly change from one caldera to another ($d = 2$ -5 km). This allows us to fix d at a representative value of 2.5 km and to vary R and H only. We implemented two groups of experiments: one with a stationary frozen-in temperature field, and the other with full time-dependent heat conduction and advection. The first group applies to the caldera collapse that occurs rapidly, and the initial thermal field has no time to diffuse. The second group considers both the collapse and the long-term postcollapse evolution, for which an account of the thermal transport is indispensable.

The experiments with a frozen-in temperature field were subdivided into two subgroups. In the first, we assumed far-field boundary velocities equal to zero (no regional compression or extension); in the second, we investigated the influence of background tectonic extension. During these experiments we assumed a typical steady state crustal geotherm corresponding to the parameters from Table 1.

The numerical experiments were started from problem-specific tests of the code, including comparisons with analytical predictions and convergence or res-

olution tests by decreasing the grid size by factor of 2, 4, and 8. The choice of the time step is ensured automatically using stability and convergence criteria derived by Marti and Cundall [1982], who have shown that the time step should be smaller than the time of propagation of elastic compressional wave through smallest grid element, Maxwell relaxation, and heat propagation time. To save computing time, we chose a resolution sufficient to resolve major border faults but not the smaller ones (second order, etc). Further grid refinement does not result in qualitative changes in the behavior of the faulted system; it only affects the width of the shear bands and the distribution of the secondary and smaller order faults, yielding infinitely refining fractal distributions with increasing resolution [Poliakov *et al.*, 1994]. In all tests with decreased grid size we observed that stress concentration zones obtained in a “low”-resolution mode coincide with fault localization zones obtained at higher resolution. Consequently, higher resolution basically allows one to obtain a more accurate fault geometry of the primary fault locations already well resolved by the lower-resolution models.

4.4.1. Caldera collapse in the absence of the regional stress field, frozen-in temperature field.

Here we investigated the relationships between three major geometric parameters of the caldera: horizontal size ($2R$), depth to the magma chamber (d), and thickness of the overpressured magma chamber (H). We studied six general cases shown in Figures 9 and 10: (1) $2R/H = 1$ (“S, small caldera”), $2R/d = 2$, (2) $2R/H = 2$ (“M, medium caldera”), $2R/d = 4$, (3) $2R/H = 2.4$ (“ML, medium-to-large caldera”), $2R/d = 4.8$, (4) $2R/H = 3$ (“L, large caldera”), $2R/d = 6$, (5) $2R/H = 5$ (“XL, very large caldera”), $2R/d = 10$, and (6) $2R/H = 15$ (“XXL, extremely large caldera”), $2R/d = 30$.

At the first stages of the large caldera case (Figures 9a and 9b, bottom) some surface uplift occurs due to an overpressured chamber. In this case, upward caldera roof bending precedes the collapse and the flexural stress concentrates at the upper corners of the chamber, resulting in the formation of inverse inclined border faults propagating from the top to the bottom of the chamber roof. The inclination of the faults is controlled by the friction angle, which determines principal failure direction in the frictional material.

Extruded by overpressure, the magma leaves the chamber and undergoes various physical and chemical modifications that, in our model, are simulated by change of the thermal conductivity, density, and mechanical strength of the magma to those of the residual ignimbrites accumulating as a surface load on the cover of the magma chamber. When this load can no longer be supported by the chamber pressure and roof strength, the chamber cover starts to flex down and subside (Figures 9a and 9b, middle). Roof bending results in the failure at the borders (in perfect agreement with our analytical estimations) and in the initiation of nor-

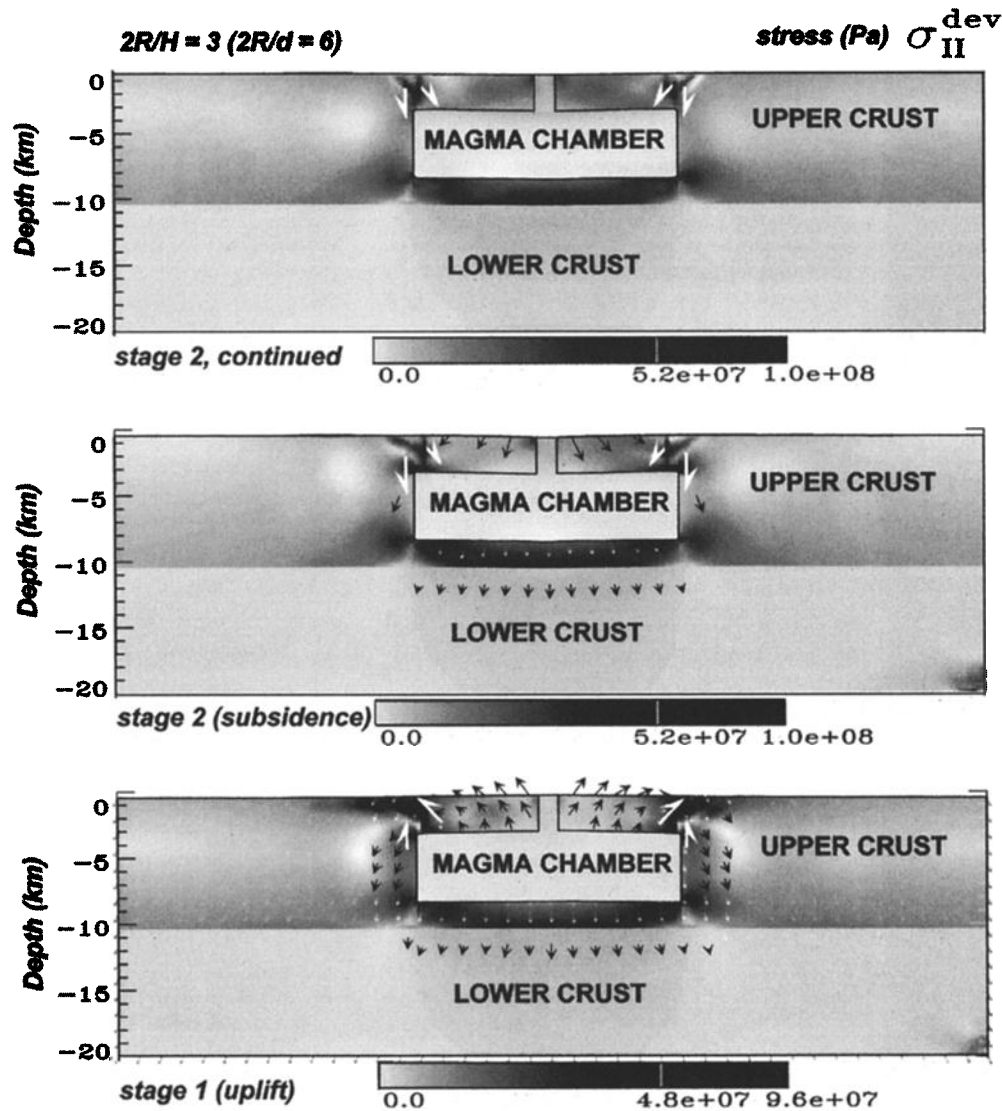


Figure 9a. Consequent phases of the caldera collapse and development of the border faults with regional tectonic stress for deviatoric shear stress distribution (second invariant of the stress tensor).

mal inclined border faults cutting through the cover, or in the reactivation of the faults formed during the upward flexure of the cover preceding the collapse. The roof slides down on the inclined faults, but this displacement is limited by the inward dipping geometry of the cover (Figures 9 and 10). This sliding is also prevented by eventual fault locking due to friction, which continuously increases with accumulation of the surface load. When sliding on the inclined faults stops but the normal load continues to grow, the roof snaps once again, but now in a more favorable vertical direction. New subvertical border faults form, allowing for "easy" piston-like subsidence. Such subsidence is no longer resisted by friction or flexural strength of the cover, and can result in an accelerated loss of the material through the central vent which may continue as long as there is a disbalance between the chamber pressure and load on

the cover and, naturally, as long as there is free space left.

The experiment in Figure 9 (L caldera) demonstrates that the inclined border faults can be formed during the uplift phase and finally shaped during the subsidence phase. The inclined faults are followed by subvertical faults that mostly start at depth and propagate upward. The inclined normal faults may be initialized (1) at the surface during the subsidence phase and propagate down to the corners of the chamber or (2) at depth during the possible uplift phase (in this case they first appear as inverse faults) and propagate upward to the surface. This particular behavior is different from what is expected on the basis of simple analytical elastic estimations, which suggest that the faults preferentially start at the surface in the uplift phase and at the depth in the subsidence phase.

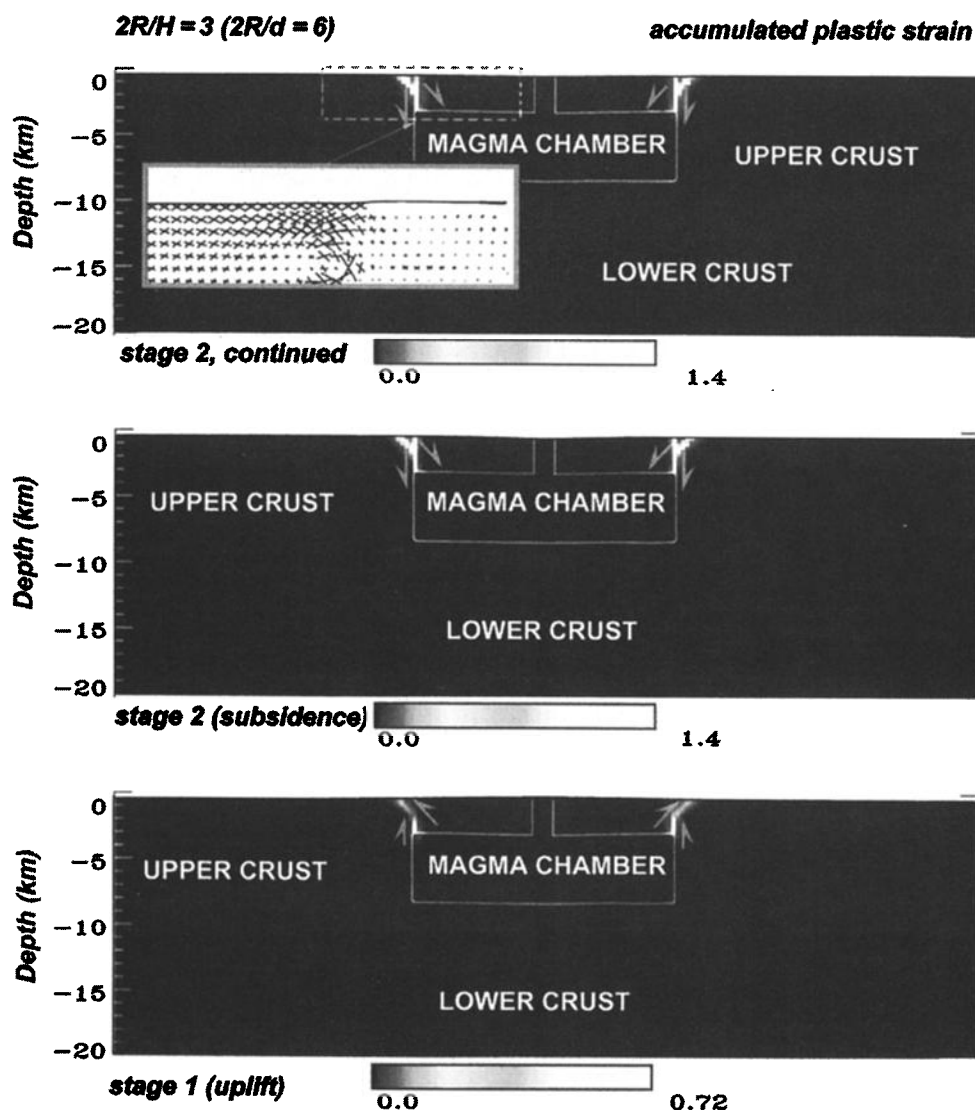


Figure 9b. Accumulated plastic strain. Constant geometric parameters are cover thickness $d = 2.5$ km, and chamber thickness $H = 5$ km. Insert on the left shows directions of the potential brittle failure around the magma chamber. Note concentrations of the actual and potential cracks at the outer side of the border. Note deviatoric stress concentrations (around 10 MPa) at the sides of the faults, resulting in nonlithostatic pressure anomalies of the same order, pressure gradients of about $\geq 10 \text{ Pa m}^{-1}$.

In the case of small $2R/d$ ratios (Figures 10a and 10b, top) the border faults cannot form since the flexural stresses in the magma chamber roof cannot exceed the brittle strength of the rocks. Starting from $(2R/d) > 4$, bending stress may come close to the critical level. In this situation, a single fault on an occasionally weaker side may appear, forming conditions for so-called trapdoor subsidence (see Figure 10b where $(2R/d) = 4.8$ and Figure 1c). It is noteworthy that this collapse mechanism could not have been reproduced assuming a commonly inferred axial symmetry. Starting from $(2R/d) = 6$, the cover continuously breaks at all sides of the caldera. Finally, when $(2R/d) > 10$, secondary zones of roof failure may also appear at the emplacements where the second derivative of the flexural

deflection, w'' , has two extreme values (or more depending on the $2R/d$ ratio) within the interval $0 < x < R$. In the experiments shown in Figures 9, 10a, and 10b, the chamber roof is not sufficiently thick in the vertical direction ($d = 2.5$ km, 10 elements \times 0.25 km) to allow one to resolve the localization of the deformation associated with the secondary extremes of the bending stress. The results of computations made for a thicker magma chamber roof ($d = 5$ km, or 20 elements) are given in Figure 10c, which clearly shows the formation of a secondary fault system associated with the flexure between the borders and center of the caldera.

4.4.2. Caldera collapse in the presence of the regional stress field. In the second group of experiments (Figure 11) we assumed that the caldera under-

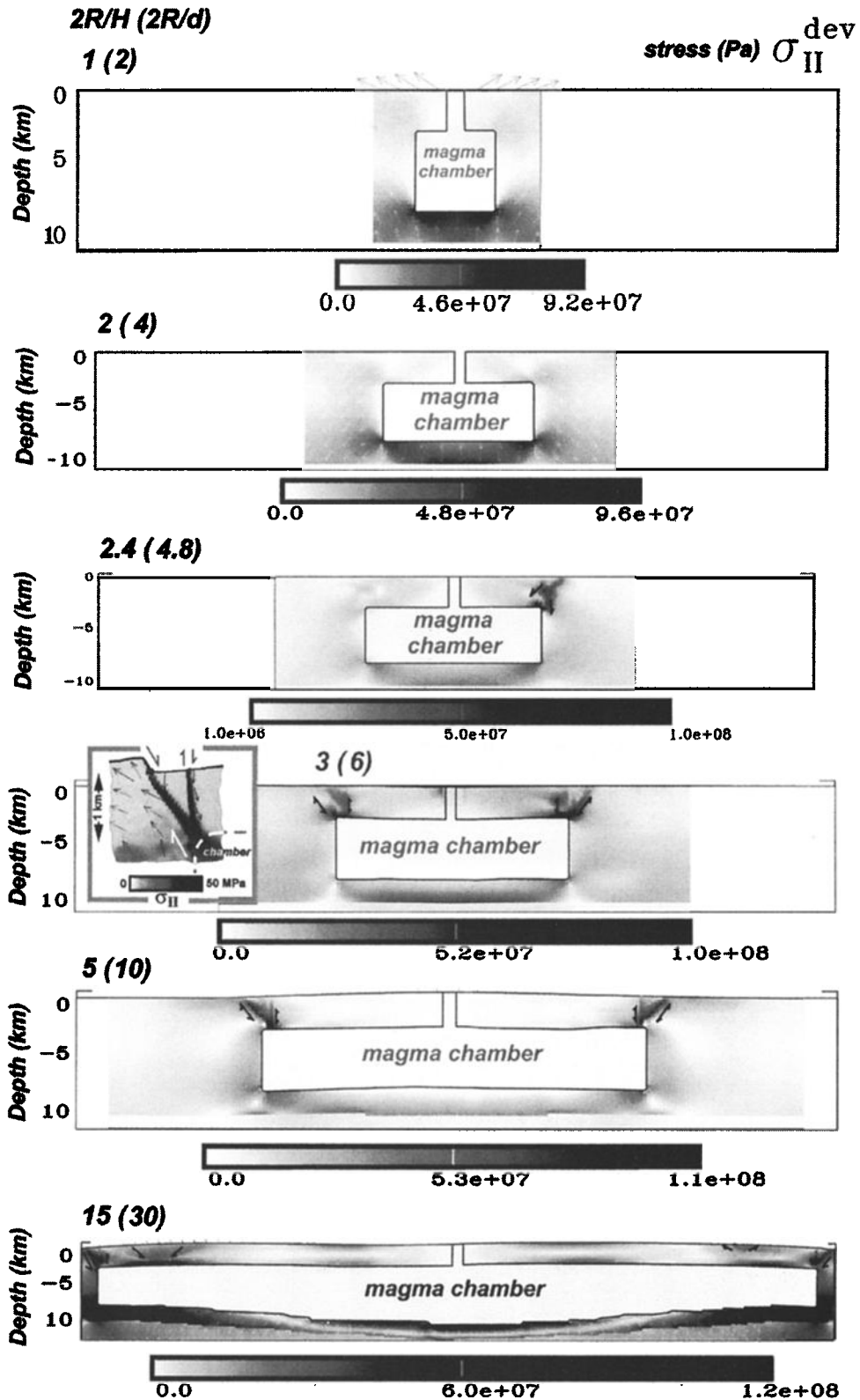


Figure 10a. Relationship between the geometric characteristics of the magma chamber and distribution of the border faults for deviatoric shear stress distribution. Effect of variation of the ratio of the caldera diameter to magma chamber thickness ($2R/H$), or thickness of the cover ($2R/d$, given in parentheses). The inset in the large caldera case ($2R/H = 3$) is obtained at a high numerical resolution. Fault geometry is clearly delineated as well as velocity field.

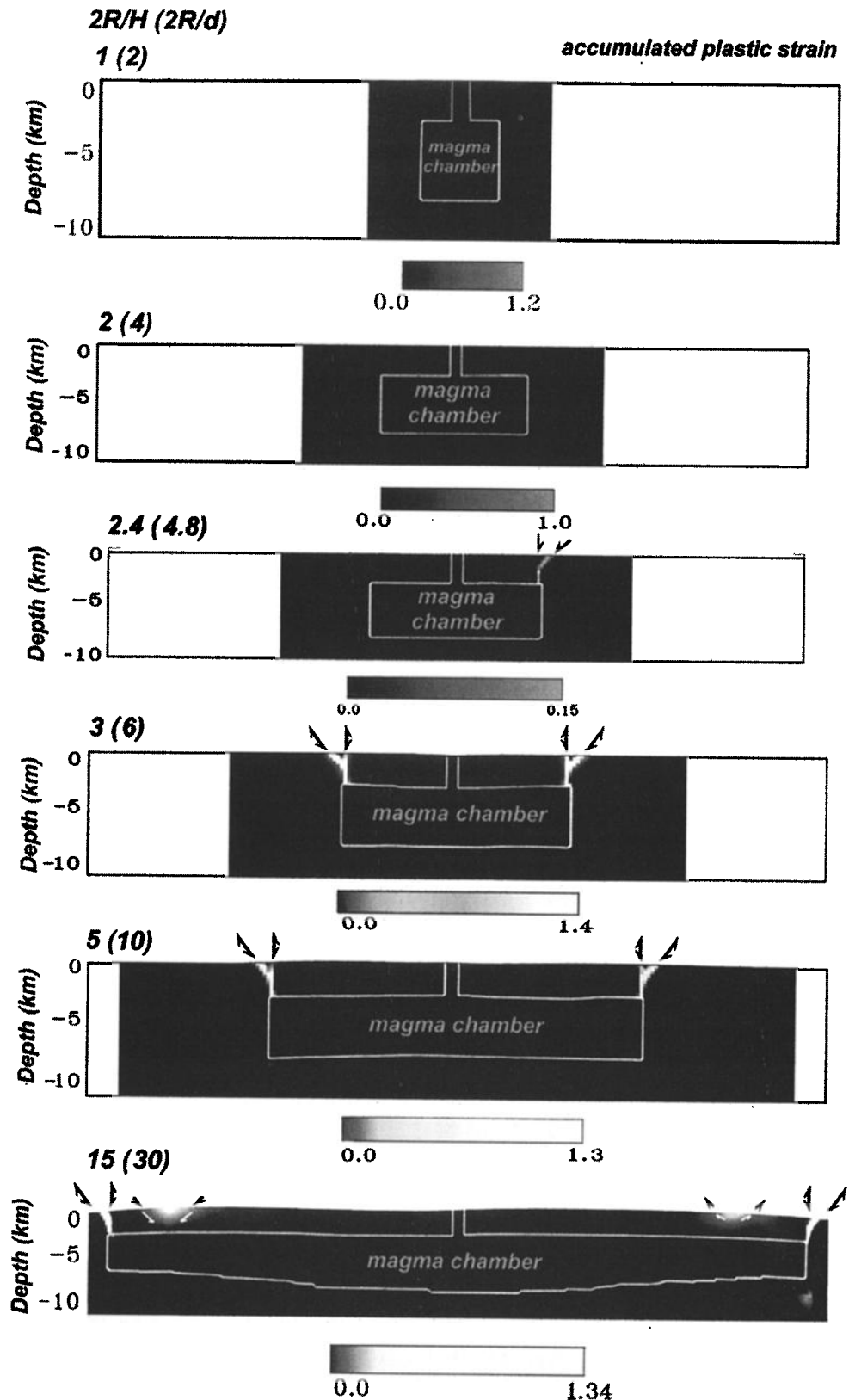


Figure 10b. Same as Figure 10a, except for accumulated plastic strain.

goes extension associated with regional tectonic deformation. This experiment is analogous to that of Figure 9 ($2R/d = 5$) except that the lateral boundary conditions now correspond to an additional far-field exten-

sion at a constant rate of 10 mm yr^{-1} . As one can see, the presence of the far-field stress can significantly modify the distribution and geometry of faulting. The regional extensional stresses shift the locations of the

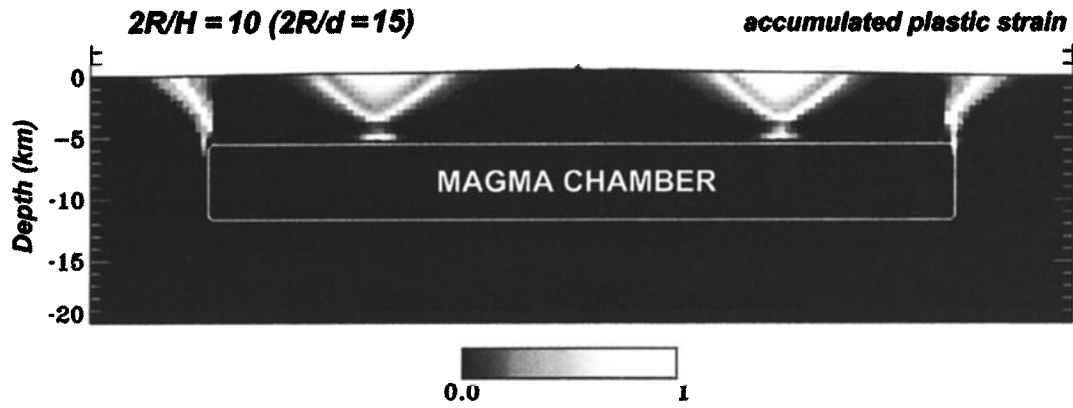


Figure 10c. Example demonstrating formation of the secondary faults at a better numerical resolution of the caldera roof, imposed by larger values of d and H , ($d = 5$ km and $H = 7.5$ km), with no regional tectonic stress. Velocity field is shown with arrows.

zones of minimal and maximal bending stresses in the magma chamber roof, leading to the primary formation of multiple faults in the proximity of the center of the caldera floor. In addition, the regional extension pro-

vokes a gradual uplift of the magma chamber and upward deformation of its bottom. This may result in a pressure rise in the magma chamber, additional magma extrusions, and uplift of the cover. We believe that

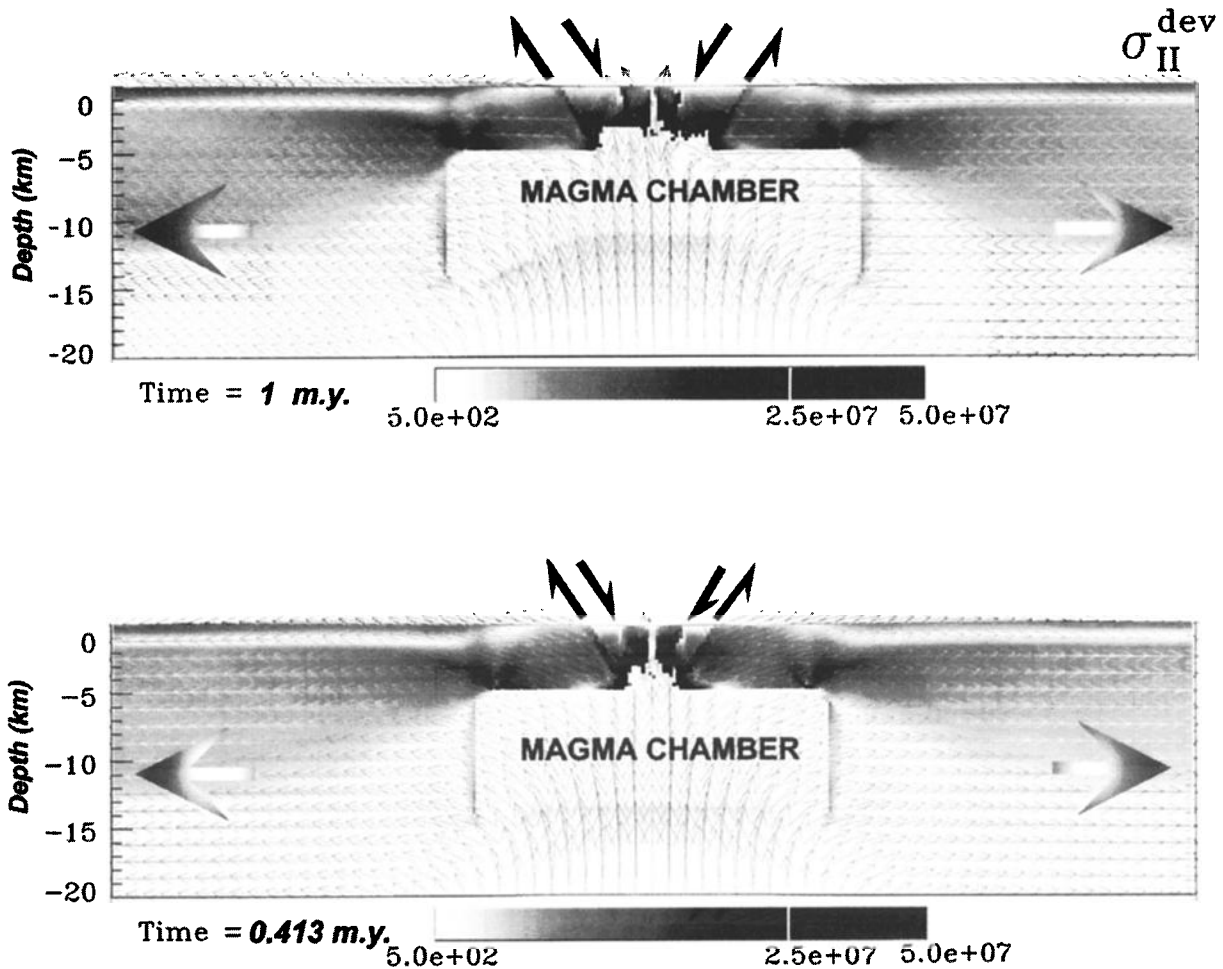


Figure 11. Development of a caldera in a regional tectonic extension field (10 mm yr^{-1} ; arrows correspond to the velocity field). Note the concentration of faults at the center of the caldera floor and the practical absence at the borders. Nonlithostatic pressure/stress reaches 5 MPa in this case. The timescale is imposed by velocity boundary conditions.

this scenario may partly explain the formation of deep-seated and intrusion-centered ore deposits. However, a detailed study of the influence of regional tectonic stresses on caldera evolution requires sufficient knowledge of the tectonic history of the adjacent regions.

4.4.3. Non-steady state thermal field and mechanical response of the caldera system. Thermal perturbation resulting from the caldera collapse may lead to the establishment of a new steady state thermal regime with a transient period that may last up to 0.5 m.y. and during which a series of thermally controlled mechanical processes may take place, significantly changing the geometry and conditions in the brittle and ductile zones surrounding the magma chamber. Two thermal effects should have major influence on the evolution of the postcollapse system: (1) heat diffusion from the hot magma body and (2) a thermal blanketing by the ignimbritic cover. The quartz-rich materials (silicic magma and the embedding crust) can easily flow by ductile creep mechanism at temperatures as low as 250-300°C. The transition from “cold” brittle behavior to “hot” ductile creep may limit the propagation of the brittle faults and cracks and thus influence the geometry of zones of brittle failure. This especially concerns the cover of the magma chamber, of which the upper part is brittle but the lower part may be ductile.

For these reasons, we implemented a third group of numerical experiments that incorporate full coupling of the heat transfer equations with mechanical equilibrium and constitutive equations. In the experiment presented in Plate 1 and Figure 12, the magma chamber has an initial temperature of 800°C. The low conductive ignimbrite layer of the cover has a “representative” thickness of 1.25 km (see Table 2 for the thermal parameters). The background geotherm in the surrounding crust corresponds to a continental geotherm with ambient temperatures of about 50-70°C at the depth of 2.5 km (chamber roof) and 150°C at 7.5 km (chamber bottom). These background values are well below the initiation level of thermally activated creep in the brittle-ductile crust, but the presence of the hot magma chamber locally increases the temperature of the embedding rock to 200-300°C at the depth of 2.5 km, and to 400°C at the depth of 7.5 km, which is sufficient to activate ductile deformation everywhere around the chamber. The magma chamber thus creates a ductile “aureole” around itself, delineated by a smoothed ovoid brittle-ductile boundary that can be considered as the “thermomechanical” geometry of the magma chamber (in contrast to more common chemical/lithological definitions). The brittle deformation (cracks and faults) will follow this boundary without penetrating inside (except possibly for major faults). The reflection of the magma heat by the ignimbrite blanket on the surface results in overheating of the lower part of the magma chamber roof, which thus becomes even more ductile. This significantly reduces the effective mechanical thickness of the roof, as well as the depth and inclination of

the border faults. In the particular case of Plate 1 and Figure 12, the presence of an ~1-km-thick ignimbrite layer results in (1) uplift of the geotherm of the brittle-ductile transition (BDT) in the magma chamber roof from the initial depth of 2.5 km (roof/chamber interface) to a depth of 1.0-1.5 km (middle of the chamber roof), (2) reduction of the flexural strength of the roof, and (3) strong modification of the length and geometry of the border faults which descend “normally” to the depth of the BDT and then split into two directions: one (major) turning around the BDT zone delineating the magma chamber, the other (minor) following the BDT boundary within the magma chamber roof. In the case presented in Plate 1 and Figure 12, thermal effects resulted in a horizontal delamination of the magma chamber cover into two subhorizontal layers divided by a zone of subhorizontal ruptures. The final geometry of the brittle zones resembles earthquake data from the Rabaul caldera in Papua New Guinea (Figure 12) [Jones and Stewart, 1997], which suggests almost exactly the same geometry. Although the ring fault geometry (inward or outward dipping faults) in the Phlegraean Field caldera has been shown to be strongly related to vertical ground motions [Troise *et al.*, 1997], earthquake hypocenters are less focused on the discontinuities, possibly due to the data or processing limitations, and comparison with our results is more difficult.

Rapid changes in the thermal regime associated with eruption and collapse result in thermoelastic stresses that may also effect the evolution of the border faults and central dome. However, this effect significantly depends on (1) the thermal history of the chamber settling and (2) the inferred rheological properties of the magma chamber roof as well as the thermal conditions at the chamber roof/magma body interface and the initial temperature of the magma. The roof of the recurrently replenished chambers should rapidly heat up, resulting in reduction of the caldera mechanical thickness and, consequently, in shallow faulting.

The general aim of the thermally coupled experiments was to demonstrate the importance of the thermal effects rather than to suggest a particular scenario of the thermal evolution. Here the important result is that they show that the “mechanical” geometry of the magma chamber (BDT boundary) is significantly controlled by temperature, in addition to the gravity-driven deformation. Hot magma creates a large ductile zone in the surrounding crust, following the geometry of the blurred thermal diffusion aureole around the chamber. In our experiments the initially rectangular magma chamber adapted its geometry and took on a rather elliptical shape. During these experiments we also tested quasi-Rayleigh-Taylor mechanisms of chamber emplacement in the brittle-ductile media. The initial hot chamber was placed in the lower crust (25 km depth) and was allowed to float up in the denser surrounds. As we could observe, even in the case of positive buoyancy, the chamber could be stopped and frozen in the

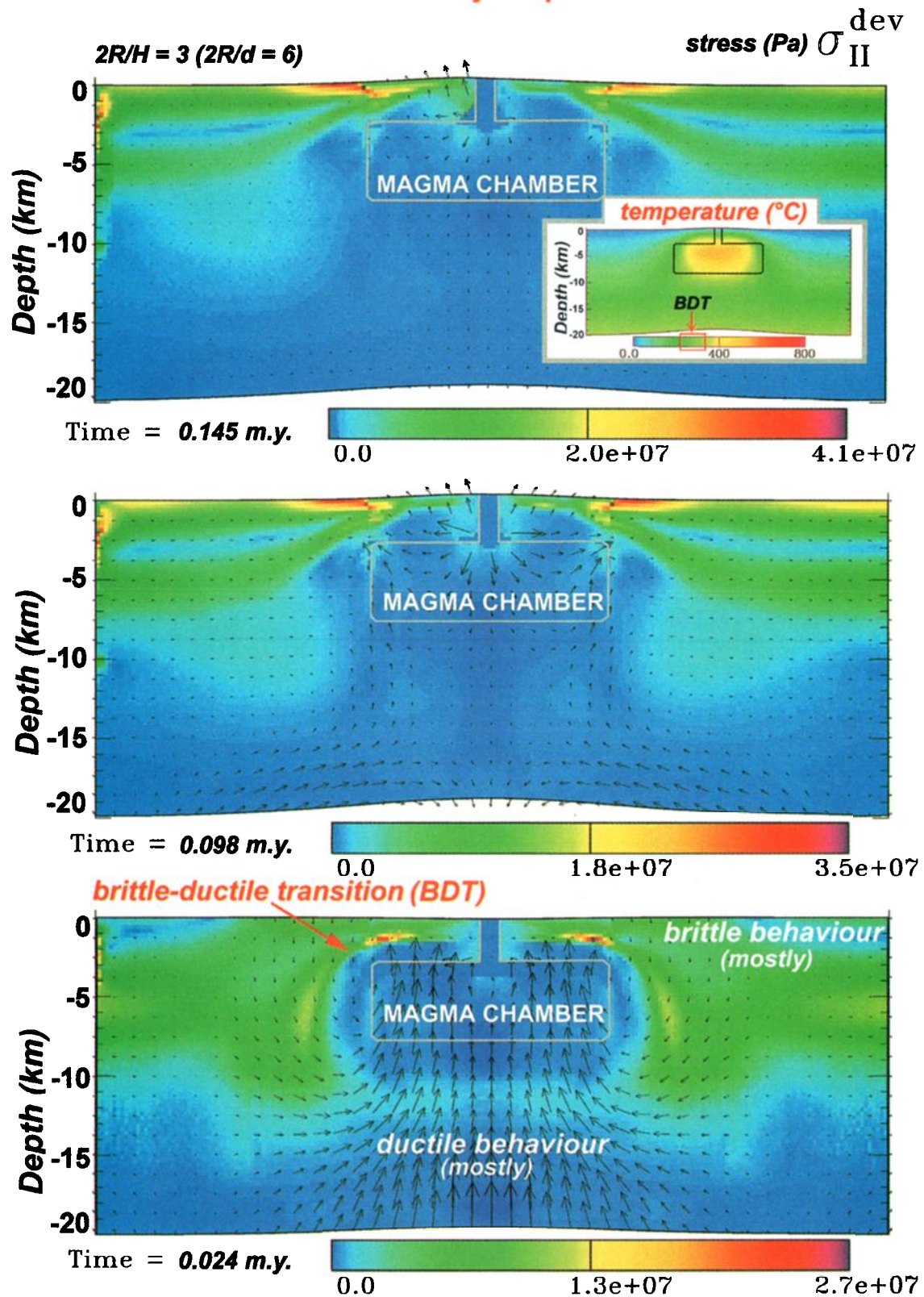
Shear stress. Thermally coupled caldera model

Plate 1. Interaction between the evolving thermal field and mechanical response of the caldera system, deviatoric shear stress distribution (second stress tensor invariant). A poorly conductive ignimbrite layer is deposited on the surface of the caldera cover. Note that the nonlithostatic stress/pressure reaches 5-10 MPa close to the faults, which exceeds the lithostatic pressure at corresponding depth. Pressure/stress gradients are of the order of several megapascals per meter. The insert shows temperature distribution.

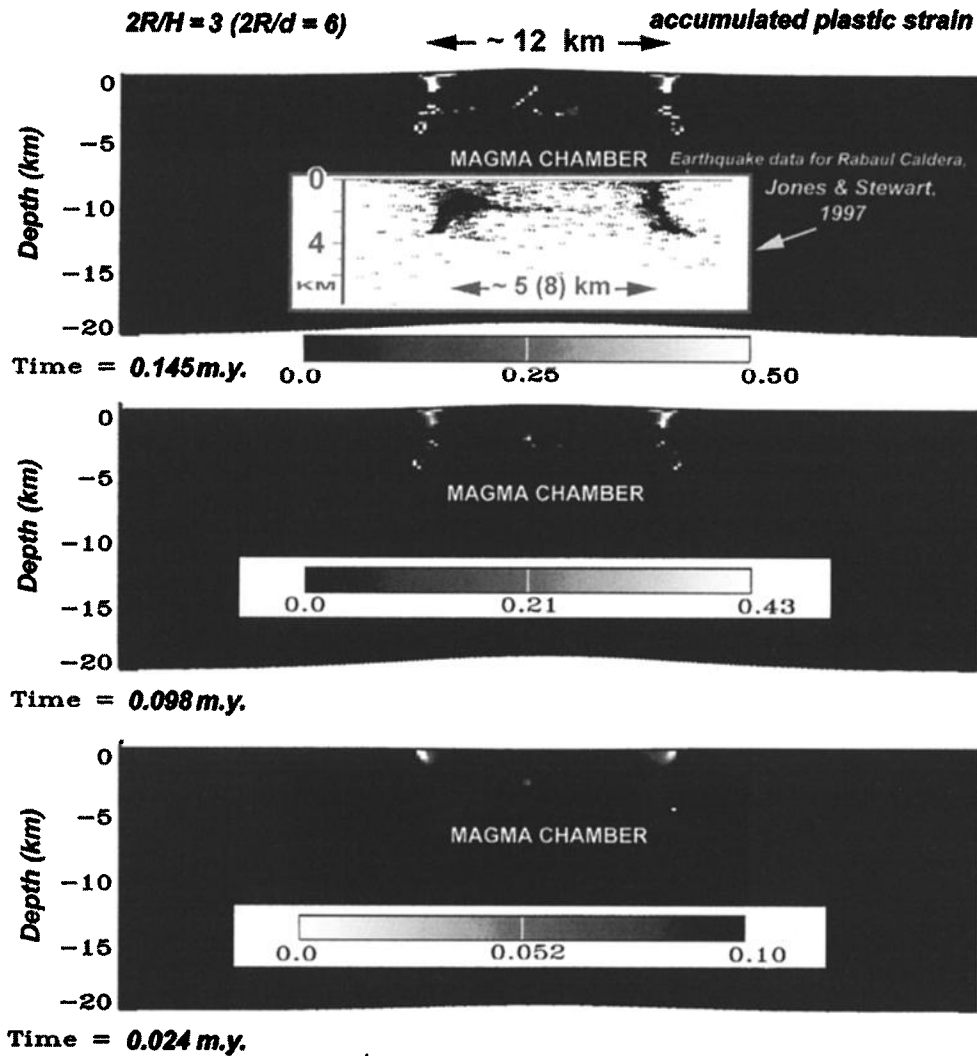


Figure 12. Accumulated plastic strain for the case shown in Plate 1. The insert shows the depth distribution of the earthquakes at Rabaul caldera [after Jones and Stewart, 1997]. Horizontal scale is slightly exaggerated to emphasize similarities in fault geometry and earthquake distribution. Rabaul caldera has planar ovoid shape of dimensions of about 5×8 km. The timescale is essentially controlled by heat diffusion rates.

brittle layer if it had insufficient thermal energy (volume, temperature) to ductilize the brittle surrounds. In any case, the roof of the chamber cover was not able to rise above 2 km depth: above this level it is difficult to ductilize the overlying rocks because of their efficient cooling through the surface. Surprisingly, this depth limit coincides with the minimal depth of the silicic magma chambers [e.g., Cubellis *et al.*, 1995; Hill *et al.*, 1998]. Another result specifically related to the problem of magma chamber emplacement was the formation of surface normal faults long before the actual arrival of the chamber at the surface. When the chamber was still at 10 km depth, the induced upward flow was able to create extensional stresses at the surface sufficient to promote faulting. The distance between these “prevolcanic” faults was controlled mainly by the

effective thickness of the competent brittle layer and not by the magma chamber geometry, just until its arrival at the surface. This result requires further investigation since it may help in understanding fundamental processes occurring in the upper crust during magma chamber emplacement.

In all experiments, stress-pressure variations (10 to 50 MPa) were predicted in the vicinity of the border faults and of the upper part of the magma chamber, even during the quasi-steady stages of caldera evolution. Thus even in the stationary regime, long after the collapse, the nonhydrostatic stress/pressures may be largely sufficient to drive fluid flow from the caldera to the outer side of the fault and overprint or disturb other circulation mechanisms (see Gaeta *et al.* [1998] for such fluid-dynamic effects in ash flow calderas).

5. Discussion and Conclusion

5.1. Summary of the Results

Our experiments have shown that the border faults of ash flow calderas can be created by two mechanisms: (1) localized stress concentrations at the borders of the caldera caused by flexure of the roof and (2) yielding of the preweakened borders under the normal load (pressure and deposits) applied to the cover. Formation of the continuous symmetric border faults (Figure 1a) connected to the magma chamber occurs at intermediate and large aspect ratios ($2R/H$) of 3 ($2R/d = 6$) and above. A single-side fault may appear at aspect ratios of ≈ 2.5 ($2R/d \approx 5$), thus leading to the so-called trapdoor caldera collapse scenario (Figure 1c). For the largest aspect ratios, $2R/d \geq 10$, the formation of secondary flexural faults also becomes possible. These coupled inclined faults could also be assimilated to funnel calderas, as outlined in Figure 1e.

With respect to previous and current elastic models our results demonstrate significant differences in predicted fault geometry, direction of fault propagation and possible crack network geometries. The use of elastic models is thus limited to rough estimations of critical aspect ratios leading to faulting.

The regional tectonic stress may change the style of the caldera evolution. An extensional far-field stress may be favorable for the occurrence of deep faulting concentrated around the center of the caldera. As long as the extension continues, the faults propagate from the center to the borders and create a wider dispersed fault zone.

Our numerical experiments predict that two types of border fault can be formed: inclined and subvertical. This prediction is supported by recent field studies (T. Druitt, personal communication, 1998). The inclined border faults can be created as a result of roof bending during the uplift or following subsidence phase. The vertical border faults are associated with the piston-like vertical movement of the cover and can be formed at the beginning of roof subsidence or even earlier, during the uplift phase. The inclined faults join the vertical ones either at the corners of the magma chamber or somewhere in the middle between the surface and the chamber (Figures 9 and 10).

The thermal anomaly induced by the thermal conductivity contrasts can cause an upward shift of the brittle-ductile transition in the magma chamber roof and around the chamber (Plate 1 and Figure 12). The density of the second-order crack-and-fracture network is maximum at the outer side of the vertical faults, directly above the fault junction zone (Figure 9b). The concentrations of second-order cracks at some depth on the outer side of the ring faults, quite interestingly, coincide with the locations of the heat flow anomalies predicted by the analytical thermal model (Figures 5 to 7).

The coupled thermomechanical model (Plate 1 and Figure 12) predicts the possibility of subhorizontal brittle

failure zones delineating the brittle and ductile parts of the magma chamber cover. These could serve as conduits for the hydrothermal fluids. This effect is caused by the poorly conductive intracaldera deposits (in addition to the partly emptied reservoir) screening the heat coming from the magma body. Such thermal insulation modifies the characteristics of the faults, resulting in geometries quite different from those usually assumed.

5.2. Implications for Economic Potential of Ash Flow Calderas

The geothermal and mineral potential of ash flow calderas primarily depends on the flow paths of hot fluids supposedly leading to mineral deposition and to anomalously hot temperatures at shallow depths. The presence of a hot magma body under a porous and fractured medium (the ignimbrite cover) should promote a convective circulation locking the downwellings around the border faults. The hot magma body and the insulating cover should also enhance forced convection through the major permeable zones (central vent and ring faults), giving lateral temperature gradients that are favorable for increased fluid velocities in the high-permeability zones, as shown by the "thermal channelization" process described by Bolton *et al.* [1996]. The insulating effect of the ash flow units would promote mushroom-shaped isotherms, often suggested in the sketchy figures explaining anomalous temperatures within caldera settings [e.g., Lipman, 1992; Arribas *et al.*, 1995; McConnel *et al.*, 1997]. It must be noted that fluid paths and temperature history at shallow depths are also dependent on surface topography.

In addition, downward bending of the caldera roof creates compressional deviatoric stresses in its upper part and extensional stresses in its lower part. These stresses may reach several megapascals, promoting important stress/pressure gradients directed downward and outward from the caldera and possibly forcing fluid circulation in that direction. Finally, stresses associated with the border faults may create constantly or repetitively active pressure differences of at least 5-10 MPa directed toward or away from the faults and thus pumping fluids and changing the porosity/permeability and crack density (e.g., Figures 10, 12 and Plate 1). The concept of fault forcing on the fluid flow and permeability of the surrounding rocks is widely accepted for active fault systems [e.g., Sibson, 1987] but is also applicable to steadily deforming systems. This fluid flow can be focalized and driven by nonhydrostatic large-scale stress/pressure gradients associated with caldera subsidence, steady roof flexure, and the general evolution of the caldera system.

Some ore deposits, such as low-sulfidation epithermal ores, are commonly found near the outer sides of the border faults of ash flow calderas. Among the numerous examples of such a puzzling tendency are the high-sulfidation epithermal deposits of the Lomilla caldera,

nested within the Rodalquilar caldera, Spain [Arribas *et al.*, 1995], and the low-sulfidation epithermal deposits of the Emperor Mine, Tavua caldera, Fiji Islands [Ahmad and Walshe, 1990]. The mineralization is associated with complex thermal fluid-dynamic effects [Hendley, 1985] and requires traps, such as small second-order cracks and fractures branching from the major fault surfaces. Thus the minerals carried with the hydrothermal flow can be easily trapped in the dense fracture network associated with the border faults (Figure 9b). This fault-associated network not only enhances "trapping" capabilities but also improves thermal exchange between the fluid and the host rocks. Moreover, the concentration of second-order cracks at the outer sides of the border faults, as well as the anomalous heat flow anomaly (Figures 6 and 7) might favor reheating of the deep fluids together with upwellings, and thus pressure drops along the outer side of the faults.

Figure 11 shows that the depth and the location of the initiated faults can be modified by the regional stress regime. In the Philippines a strong extensional regional stress regime before the late Miocene led to the formation of porphyry-copper deposits (deep-seated mineralization clustered in a fractured network) in districts where epithermal gold (shallow-seated mineralized veins) appeared in abundance after this period, when extension was only weak [Mitchell and Balce, 1990]. Some intrusion-centered ore deposits are attributed to a "telescoping" event, where erosion would be the driving mechanism for juxtaposing these two different styles of ore deposit [Sillitoe, 1994]. According to our results, erosion could bring both types of mineralization to the surface if the regional tectonic regime is sufficiently modified (e.g., from high to weak extension) during the lifetime of the hydrothermal system related to the magmatic structure.

5.3. Discussion

In our thermomechanical model, where the intrachamber pressure is kept constant, the outside pressure increases due to the growing normal load of the surface deposits. It is possible that roof collapse can also be caused by the suction effect due to possible pressure drop in the chamber after rapid degassing of the magma following the opening of the central vent (T. Druitt, personal communication, 1998). For this study the origin of the pressure difference does not change the mechanisms of the caldera collapse.

We used a full 2-D Cartesian model with no axial symmetry. Although such a model may predict somewhat exaggerated stresses with respect to 3-D models [e.g., van Wees and Cloetingh, 1996], it has been shown from analytical studies [Timoshenko and Woinowsky-Krieger, 1959] that for cylindrical bodies with a radius several times greater than height, this difference should be < 10-30%. This uncertainty is considerably smaller than possible differences between stresses computed us-

ing realistic brittle rheology and those obtained from commonly used elastic stress predictions [Buck, 1997; Gerbault *et al.*, 1998]. Compared to widely used 2-D curvilinear axisymmetric models, our model can reproduce differences between the geometries and fault distributions and uplift/subsidence on the opposite sides of a caldera (e.g., trapdoor subsidence). In addition, many calderas are strongly elongate in the horizontal plane and are also intersected by linear tectonic fault or are found in uniaxial tectonic extension fields. This limits the application of axisymmetric models.

One can question whether the sharp geometry of the magma chamber edges used in the experiments of Figures 9 and 10 could significantly affect fault initiation. A smoother geometry could be easily incorporated, but existing geological or geophysical data do not really allow for a better choice of the corner geometry. For example, the elliptic shapes typically found in the literature are often based on hypothetical considerations. Nevertheless, in most of the experiments shown here, the primary inclined faults were initialized by upward roof flexure, starting at the surface and then propagating downward; the peculiarities of the border geometry would have no influence on this. It is also seen that the faults initialized from below do not start at the chamber corner but at some distance from it (Figure 10). Thus it is unlikely that the geometry of the chamber corners significantly contributes to fault initialization. Our preliminary tests have shown that the faults appear at the same aspect ratios for effectively spheroidal or elliptical chambers (compare also with rounded chambers in Plate 1).

Our model accounts for various magma chamber shapes, but we did not really tackle the problem of how such magma chamber geometries can be emplaced in the shallow crust. As was mentioned in the modeling section, we conducted a number of preliminary experiments on this problem and obtained quite encouraging results showing that (1) an ascending magma chamber may create surface faults long before its emplacement close to the surface and (2) the depth of a silicic magma reservoir is largely controlled by the brittle surface layer, not necessarily by the level of neutral buoyancy as commonly suggested [Ryan, 1987; Lister and Kerr, 1991]. Nevertheless, a more complete approach would be needed to incorporate (1) the magma emplacement within the crust, (2) the formation of the magma reservoir, and then (3) the formation and evolution of a caldera following the explosive eruption.

In the numerous cases of a large and thick silicic magma reservoir settled at a shallow level our thermomechanical approach helps to constrain the geometry of the mechanical magma chamber. Usually, magmatic reservoirs are defined thermally or compositionally: for example, the thermal definition implies that the reservoir is delimited by a specific isotherm roughly corresponding to the boundary between the "mushy" zones and the embedding rocks. In our model the heat diffu-

sion from the hot magma body allows us to determine the geometry of a ductile aureole around the chamber. This aureole is delimited by a brittle-ductile transition (BDT) contour within which the magma is able to inflate or be replenished. Brittle faults, and especially fractures, can be formed only outside the BDT contour. The BDT contour can be relatively insensible to changes in the bulk reservoir geometry until very significant changes occur in magmatic activity but can be quite affected by changes in the thermal regime or fluid content that modify the mechanical properties of the rocks.

Another result of this study suggests that it is not always necessary to refer to the complexity of the magmatic systems to explain some of their complex surface signatures, for example, nested calderas. We have shown that without any additional complications to the model, secondary faults embedded within border faults can be easily created in large aspect ratio calderas. Of course, the reader should keep in mind that we considered only simplified geometries in our model that yielded symmetrical nested structures, which are rarely found in the field (see, however, the case of the San Juan calderas cluster [Steven and Lipman, 1976]).

Appendix A: Caldera Snapping

Assuming axial symmetry in 2-D Cartesian plane, we can consider a semicaldera with radius R and roof thickness d (Figure 3). Neglecting the horizontal forces, we obtain the following simple 2-D biharmonic equilibrium equation for the chamber roof:

$$\nabla^2[D(x)\nabla^2w] = \nabla^2[D(x)w''] = P(x), \quad (\text{A1})$$

where D is the flexural rigidity and w'' is the second spatial derivative of the vertical deflection of the roof w . The normal load on the sides of the roof (overpressure p and/or deposits) $P(x)$ is equal to $-p + \rho gh$, where ρ is the material density and h is the deposit thickness (Table 2). As a first step, the normal load can be replaced with an integral action of a cutting force F applied at the center (Figure 3), whereupon (A1) becomes, for $x < R$,

$$\nabla^2[D(x)w''] = 0. \quad (\text{A2})$$

This equation requires four boundary conditions: (1) the effective load of deposits at the center of the roof ($x = R$) equals F ; (2) the tip of the free edge is not curved; (3) the border end of the cover (at $x = 0$) is fixed before the snapping/faulting occurs; and (4) the fixed end is not inclined. Conditions 1-4 can be written as follows:

$$F|_R = F \approx \int_0^R P(x)dx; w''|_R = 0; w|_0 = 0; w'|_0 = 0. \quad (\text{A3})$$

Assuming for simplicity that $D(x) = \text{const} = D$, we get $w'''' = 0$, that is, $w'''' = C_1 = \text{const}$. Since the first

derivative of the flexural moment M ($M = -Dw''$), M' , equals F , we get $w'''' = -M'/D = -F/D$, which yields, using the boundary condition 2, $w'' = -F(x - R)/D$. Using the boundary conditions 3-4, we get

$$w = Fx^2(R - x/3)/2D. \quad (\text{A4})$$

The elastic flexural stress σ_e in the rigid core of the cover can be written as

$$\begin{aligned} \sigma_{xx} &= -\sigma_{xx}^e = \varepsilon_{xx}E(1 - \nu^2)^{-1} \\ &= E(1 - \nu^2)^{-1}(y - 0.5T_e)w'' \end{aligned} \quad (\text{A5})$$

or

$$\sigma_{xx} = \frac{-F}{D} \frac{E}{1 - \nu^2} (y - 0.5T_e)(x - R). \quad (\text{A6})$$

The material starts to “snap” when the bending stress σ_e reaches the limit of plastic (brittle) yielding at depth y , σ_γ :

$$\sigma_e = \sigma_\gamma = \vartheta(\sigma_n - \sigma_p) + \sigma_o, \quad (\text{A7})$$

where $\sigma_n - \sigma_p$ is the difference between the normal and the pore pressure, ϑ is the internal coefficient of friction of the material, typically $\vartheta \approx tg(\pi/6)$, and σ_o is the cohesive rock strength, typically 10 to 20 MPa at the surface and 20-30 to 40-60 MPa at the bottom.

Since the local radius of curvature of the cover is $r_{xy} \approx -(w'')^{-1} = -D/F(x - R)$, we can estimate the critical value of the radii of curvature at which the plate is no longer elastic and starts to snap, i.e., $r_{xy} = -D/F_c(x - R)$, where the critical edge force F_c is found from equating the condition of plastic yielding (A7) to the expression for stress (A6). As follows from this expression, the minimum radius of curvature is reached at the border of the cover, and thus it is here that the cover will tend to snap. The critical curvature is conditioned by three controllable parameters: the rigidity D , which can be computed from the known thickness of the cover d ; the estimable value of the edge force F , which is proportional to the normal load (deposits and overpressure); and the known radius R of the caldera.

Commonly inferred values for E and ν are 6.58×10^{10} to 8×10^{10} N m⁻², and 0.25, respectively [e.g., Watts, 1978; Turcotte and Schubert, 1982]. Assuming $T_e \approx d = 2.5 - 5$ km, this will yield the following values of D :

$$D = \frac{ET_e^3}{12(1 - \nu^2)} = 10^{19} - 10^{20} \text{ N m}. \quad (\text{A8})$$

Taking commonly inferred values of the brittle rock strength at the surface (5-10 to 20 MPa) we can estimate the value of the critical curvatures leading to formation of the border faults. Assuming that $\sigma_e = \sigma_\gamma$ at $x = 0$, we get

$$F_c = 2\sigma_\gamma D(1 - \nu^2)/(ET_e R) = \sigma_\gamma T_e^2/(6R). \quad (\text{A9})$$

Considering a homogeneously distributed load $P(x) = P$, instead of the edge force F , we can obtain

the solution of (1) in the form [Turcotte and Schubert, 1982]

$$w = PD^{-1}x^2(x^2/24 - Rx/6 + R^2/4), \quad (\text{A10})$$

which yields

$$w'' = PD^{-1}(x^2/2 - Rx + R^2/2). \quad (\text{A11})$$

The bending stress at the surface equals:

$$\sigma = 6d^{-2}P(x^2/2 - Rx + R^2/2),$$

which has a maximum value $3P(R/d)^2$ at $x = 0$ (border). Consequently, the normal load P sufficient to break the cover at the border can be $3(R/d)^2$ times lower than its brittle strength:

$$\sigma_e/P = 3(R/d)^2. \quad (\text{A12})$$

Appendix B: Heat Refraction Within Caldera Settings

The model is based on the solution of dimensionless thermal diffusion equation in Cartesian geometry. The caldera extends from the surface to a depth of 1, which stands for the base of the ash flow units (Figure 4). A constant unit heat flux ($= 1$) is imposed as a lateral condition at $x \rightarrow \pm\infty$, which is equivalent to a homogeneous heat flux condition far away from the caldera within the whole depth interval $0 \leq z < 1$. The thermal perturbations are studied only in the domain $z < 1$, because with $z > 1$ these perturbations will be rapidly damped away due to the constant heat flux condition at infinity. There are no heat sources in the model. Border faults (or quartz-rich veins) are vertical and symmetrically located at $a < |x| < b$, where $x = 0$ is the center of the caldera. Thermal conductivity is k_f in the quartz-rich fault and k_i within the ash flow tuffs. They are nondimensionalized using the value for the host rocks $k_1 = 1$. Several cases for fault widths $fw = (b - a)$, conductivity values, and conductivity ratios $r_k = k_f/k_i$ have been investigated. The steady state heat equation in Cartesian geometry can be written as follows:

$$\Delta T(x, z) = 0, \quad (\text{B1})$$

where $T(x, z)$ is 2-D temperature distribution. Taking T_i , T_f , and T_{ex} as the temperature fields inside the ash flow caldera ($|x| \leq a$), within the ring fault ($a \leq |x| \leq b$), and outside the caldera ($|x| \geq b$), respectively, the surface temperature is kept equal to zero and the bottom temperature equals 1 far from the caldera as a consequence of the lateral constant heat flow condition at infinity:

$$T_i(x, z = 0) = T_f(x, z = 0) = T_{ex}(x, z = 0) = 0, \quad (\text{B2})$$

$$\lim_{x \rightarrow \infty} k_1 \frac{\partial T_{ex}}{\partial z}(x, z) = 1. \quad (\text{B3})$$

Owing to symmetry, there is no horizontal temperature gradient at $x = 0$, and due to continuity, temperatures and horizontal heat flow through the vertical interfaces ($|x| = a$ and $|x| = b$) must be equal. Moreover, temperature is supposed to increase with depth throughout the whole area of Figure 4:

$$\frac{\partial T}{\partial z}(x, z) > 0. \quad (\text{B4})$$

Despite these assumptions, one condition is still missing for solving the heat equation. For this we have imposed a final condition at the surface and at the center of the caldera:

$$\lim_{a \gg 1} k_i \left(\frac{\partial T_i}{\partial z} \right) (x = 0, z = 0) = 1. \quad (\text{B5})$$

This condition is valid only for large calderas. With such geometries the isotherms are locally disturbed at the caldera borders but reach a constant heat flux state far away from them, i.e., not only at infinity but also at the caldera center $x = 0$. Even for very strong ($r_k = 30$) conductivity ratios, the constant heat flux condition at the center is valid within only 5% error where caldera diameters are > 4 times caldera thickness. For a representative conductivity ratio of $r_k = 4$ and for the same caldera diameter, the error is $< 3\%$.

In Cartesian geometry the solution for temperature is dimensionless and can be expressed via Fourier series (where q_m are wave numbers and a_m , b_m and c_m are Fourier coefficients) as

$$T_i(x, z) = \sum_{m=0}^{\infty} a_m \cosh(q_m x) \sin(q_m z) + G_{i.z}, \quad |x| \leq a \quad (\text{B6})$$

$$T_f(x, z) = \sum_{m=0}^{\infty} b_m \cosh(q_m x) \sin(q_m z) + G_{f.z}, \quad a \leq |x| \leq b \quad (\text{B7})$$

$$T_{ex}(x, z) = \sum_{m=0}^{\infty} c_m \exp(-q_m x) \sin(q_m z) + G_{e.z}, \quad |x| \geq b, \quad (\text{B8})$$

where G_i , G_f , and G_e are vertical gradients, G_e and G_i being constants. Because temperature is not disturbed away from the caldera, we must have $G_e = 1$. Fourier series can also be used for the second terms (with three other Fourier coefficients):

$$G_{i.z} = \sum_{m=0}^{\infty} \alpha_m \sin(q_m z), \quad G_{f.z} = \sum_{m=0}^{\infty} \beta_m \sin(q_m z),$$

$$G_{e.z} = \sum_{m=0}^{\infty} \gamma_m \sin(q_m z). \quad (\text{B9})$$

The conditions $\partial T / \partial z > 0$ and $G_e = 1$ are verified using

$$q_m = \frac{(2m+1)\pi}{2}, \quad \gamma_m = \frac{8(-1)^m}{\pi^2(2m+1)^2}. \quad (\text{B10})$$

Using both boundary and continuity conditions, we can obtain all Fourier coefficients:

$$a_m = \frac{\gamma_m(1 - \frac{k_1}{k_i})}{(1 - \frac{k_1}{k_f})\cosh(q_m a) + \frac{k_1}{k_f}\cosh(q_m b) + \frac{k_1}{k_i}\sinh(q_m b)} \quad (\text{B11})$$

$$b_m = a_m \frac{k_i}{k_f}, \quad c_m = -a_m \frac{k_i}{k_1} \sinh(q_m b) \exp(q_m b) \quad (\text{B12})$$

$$\alpha_m = \gamma_m \frac{k_1}{k_i}, \quad \beta_m = \alpha_m + a_m \cosh(q_m a) (1 - \frac{k_2}{k_f}), \quad (\text{B13})$$

where $k_1 = 1$. This solution enables computations of steady-state heat refraction effects in two dimensions, and is suited for the case of large calderas. Analytical expressions from (B6) to (B13) have been modified to avoid summing positive exponential terms, and an accuracy of 0.1% was easily reached with < 5000 terms in the series. Details of the results are shown in Figures 5, 6, and 7.

Acknowledgments. Our work benefited from discussions with T. H. Druitt, C. Jaupart, E. Marcoux, and J. P. Milési. We are particularly grateful to P. Delaney, F. Dobran, and G. De Natale for their highly constructive reviews. The modeling gained a lot from the advantages of the last modifications in the PARAVOZ code introduced in real-time-mode interaction with A. Poliakov, one of the authors of the code (the original kernel of this code was derived in 1992 by him and Y. Podladchikov from the FLAC[®] algorithm). Since 1992, E. Burov's collaboration with A. Poliakov has resulted in the joint development of a "tectonic" version of this code (power law materials, heat transfer, erosion). Some figures were prepared using the public domain graphics package GMT by Wessel and Smith. We thank Sir Patrick Skipwith for proofreading the final text and English editing. This is BRGM publication 99015.

References

- Ahmad, M., and J.L. Walshe, Wall-rock alteration at the Emperor gold-silver telluride deposit, Fiji, *Aust. J. Earth Sci.*, *37*, 189-199, 1990.
- Arribas, A., Jr., C.G. Cunningham, J.J. Rytuba, R.O. Rye, W.C. Kelly, M.H. Podwysocki, E.H. McKee, and R.M. Tosdal, Geology, geochronology, fluid inclusions, and isotope geochemistry of the Rodalquilar gold alunite deposit, Spain, *Econ. Geol.*, *90*, 795-822, 1995.
- Ascolese, E., A. Aurisicchio, M. Briggs-Smith, D.G. Mita, G. Perna, S. Rossi, and F.S. Gaeta, Thermodynamics of water-permeated unwelded pyroclasts, 2: Non-equilibrium properties, *J. Volcanol. Geotherm. Res.*, *57*, 235-251, 1993.
- Avouac, J.P., and E.B. Burov, Erosion as a driving mechanism of intracontinental mountain growth, *J. Geophys. Res.*, *101*, 17,747-17,769, 1996.
- Bailey, R.A., G.B. Dalrymple, and M.A. Lamphere, Volcanism, structure, and geochronology of Long Valley caldera, Mono County, California, *J. Geophys. Res.*, *81*, 725-744, 1976.
- Bianchi, R., A. Coradini, C. Federico, G. Giberti, P. Lanciano, J.P. Pozzi, G. Sartoris, and R. Scandone, Modeling of surface deformation in volcanic areas: The 1970-1972 and 1982-1984 crises of Campi Flegrei, Italy, *J. Geophys. Res.*, *92*, 14,139-14,150, 1987.
- Bolton, E.W., A.C. Lasaga, and D.M. Rye, A model for the kinetic control of quartz dissolution and precipitation in porous media with spatially variable permeability: Formulation and examples of thermal convection, *J. Geophys. Res.*, *101*, 22,157-22,187, 1996.
- Brace, P., and D.L. Kohlstedt, Limits on lithospheric stress imposed by laboratory modeling, *J. Geophys. Res.*, *85*, 6248-6252, 1980.
- Buck, R., Bending thin lithosphere causes localized "snapping" and not distributed "crunching": Implications for abyssal hill formation, *Geophys. Res. Lett.*, *24*, 2531-2534, 1997.
- Burov, E.B., L.I. Lobkovsky, S. Cloetingh, and A.M. Nikishin, Continental lithosphere folding in central Asia, part 2, Constraints from gravity and topography, *Tectonophysics*, *226*, 73-87, 1993.
- Byerlee, J.D., Friction of rocks, *Pure Appl. Geophys.*, *116*, 615-626, 1978.
- Campos-Enriquez, J.O., and V.H. Garduño-Monroy, Los Azufres silicic center (Mexico): Inferences of caldera structural elements from gravity, aeromagnetic, and geoelectric data, *J. Volcanol. Geotherm. Res.*, *67*, 123-152, 1995.
- Carter, N.L., and M.C. Tsenn, Flow properties of continental lithosphere, *Tectonophysics*, *36*, 27-63, 1987.
- Chéry, J., A. Bonneville, J.P. Vilotte, and D. Yuen, Numerical modeling of caldera dynamical behaviour, *Geophys. J. Int.*, *105*, 365-379, 1991.
- Chesner, C.A., and W.I. Rose, Stratigraphy of the Toba tuffs and the evolution of the Toba caldera complex, Sumatra, Indonesia, *Bull. Volcanol.*, *53*, 343-356, 1991.
- Clauser, C., and E. Huenges, Thermal conductivity of rocks and minerals, in *Rock Physics and Phase Relations: A Handbook of Physical Constants, AGU Ref. Shelf*, vol 3, edited by T.J. Ahrens, pp. 105-126, AGU, Washington, D.C., 1995.
- Clemens, J.D., Granitic magma dynamics, *J. Geol. Soc. London*, *155*, 814-851, 1998.
- Cole, J.W., S.J.A. Brown, R.M. Burt, S.W. Beresford, and C.J.N. Wilson, Lithic types in ignimbrites as a guide to the evolution of a caldera complex, Taupo volcanic center, New Zealand, *J. Volcanol. Geotherm. Res.*, *80*, 217-237, 1998.
- Corrado, G., S. De Lorenzo, F. Mongelli, A. Tramacere, and G. Zito, Surface heat flow density at the Phlegraean Fields caldera (southern Italy), *Geothermics*, *27*, 469-484, 1998.
- Cubellis, E., M. Ferri, and G. Luongo, Internal structure of the Campi Flegrei caldera by gravimetric data, *J. Volcanol. Geotherm. Res.*, *65*, 147-156, 1995.
- Cundall, P.A., Numerical experiments on localization in frictional materials, *Ing. Arch.*, *59*, 148-159, 1989.
- Cundall, P., and B. Board, A microcomputer program for modeling large-strain plasticity problems, in *Numerical Methods in Geomechanics (Proceedings of the 6th International Conference, Innsbruck, Austria, April 1988)*, pp. 2101-2108, A. A. Bakema, Rotterdam, 1988.
- De Natale, G., S.M. Petrazzuoli, and F. Pinque, The effect of collapse structures on ground deformations in caldera, *Geophys. Res. Lett.*, *24*, 1555-1558, 1997.
- Dobran, F., and P. Papale, Magma-water interaction in closed systems and application to lava tunnels and volcanic conduits, *J. Geophys. Res.*, *98*, 14,041-14,058, 1993.
- Druitt, T.H., and V. Francaviglia, Caldera formation on Santorini and the physiography of the island in the late Bronze Age, *Bull. Volcanol.*, *54*, 484-493, 1992.
- Druitt, T.H., and R.S.J. Sparks, On the formation of calderas during ignimbrite eruptions, *Nature*, *310*, 679-681, 1984.

- Elder, J., *Geothermal Systems*, 508 pp., Academic, San Diego, Calif., 1981.
- Gaeta, F.S., G. De Natale, F. Peluso, G. Mastrolorenzo, D. Castagnolo, C. Troise, F. Pingue, D.G. Mita, and S. Rossano, Genesis and evolution of unrest episodes at Campi Flegrei caldera: The role of thermal fluid-dynamical processes in the geothermal system, *J. Geophys. Res.*, *103*, 20,921-20,933, 1998.
- Gerbault, M., A.N.B. Poliakov, and M. Daignieres, Prediction of faulting from the theories of elasticity and plasticity: What are the limits?, *J. Struct. Geol.*, *20*, 301-320, 1998.
- Goff, F., and J.N. Gardner, Evolution of a mineralized geothermal system, Valles caldera, New Mexico, *Econ. Geol.*, *89*, 1803-1832, 1994.
- Gudmundsson, A., J. Marti, and E. Turon, Stress fields generating ring faults in volcanoes, *Geophys. Res. Lett.*, *24*, 1559-1562, 1997.
- Guillou-Frottier, L., C. Jaupart, J.-C. Mareschal, C. Gariepy, G. Bienfait, L.Z. Cheng, and R. Lapointe, High heat flow in the Trans-Hudson Orogen, central Canadian Shield, *Geophys. Res. Lett.*, *23*, 3027-3030, 1996.
- Hallinan, S., and G. Brown, Incremental collapse and stratocone growth within a funnel-shaped caldera, Guayabo, Costa Rica, *J. Volcanol. Geotherm. Res.*, *67*, 101-122, 1995.
- Henley, R.W., The geothermal framework of epithermal deposits, in *Geology and Geochemistry of Epithermal Systems*, edited by B.R. Berger and P.M. Bethke, *Rev. Econ. Geol.*, *2*, 1-24, 1985.
- Hill, D.P., M.L. Sorey, W.L. Ellsworth, and J. Sass, Scientific drilling continues in Long Valley caldera, California, *Eos Trans. AGU*, *79*, 429, 1998.
- Jones, R.H., and R.C. Stewart, A method for determining significant structures in a cloud of earthquakes, *J. Geophys. Res.*, *102*, 8245-8254, 1997.
- Kirby, S.H., and A.K. Kronenberg, Rheology of the lithosphere: Selected topics, *Rev. Geophys.*, *25*, 1219-1244, 1987.
- Kohlstedt, D.L., B. Evans, and S.J. Mackwell, Strength of the lithosphere: Constraints imposed by laboratory experiments, *J. Geophys. Res.*, *100*, 17,587-17,602, 1995.
- Lee, T.C., and T.L. Henyey, Heat flow refraction along dissimilar media, *Geophys. J. R. Astron. Soc.*, *39*, 319-333, 1974.
- Lipman, P.W., The roots of ash flow calderas in western North America: Windows into the top of granitic batholiths, *J. Geophys. Res.*, *89*, 8801-8841, 1984.
- Lipman, P.W., Ash flow calderas as structural controls of ore deposits—Recent work and future problems, *U.S. Geol. Soc. Bull.*, *2012*, L1-L12, 1992.
- Lipman, P.W., Subsidence of ash flow calderas: Relation to caldera size and magma-chamber geometry, *Bull. Volcanol.*, *59*, 198-218, 1997.
- Lister, J.R., and R.C. Kerr, Fluid-mechanical models of crack propagation and their application to magma transport in dykes, *J. Geophys. Res.*, *96*, 10,049-10,077, 1991.
- Lobkovsky, L.I., and V.I. Kerchman, A two-level concept of plate tectonics: Application to geodynamics, *Tectonophysics*, *199*, 343-374, 1992.
- Luongo, G., E. Cubellis, F. Obrizzo, and S.M. Petrazuolli, The mechanics of the Campi Flegrei resurgent caldera—a model, *J. Volcanol. Geotherm. Res.*, *45*, 161-172, 1991.
- Mahood, G.A., Geological evolution of a pleistocene rhyolitic center-Sierra la Primavera, Jalisco, Mexico, *J. Volcanol. Geotherm. Res.*, *8*, 199-230, 1980.
- Marti, J., and P.A. Cundall, Mixed discretization procedure for accurate solution of plasticity problems, *Int. J. Numer. Methods Anal. Methods Geomech. Eng.*, *4*, 153-177, 1982.
- McConnel, V.S., J.W. Valley, and J.C. Eichelberger, Oxygen isotope compositions of intracaldera rocks: Hydrothermal history of the Long Valley caldera, California, *J. Volcanol. Geotherm. Res.*, *76*, 83-109, 1997.
- Mitchell, A.H.G., and G.R. Balce, Geological features of some epithermal gold systems, Philippines, *J. Geochem. Explor.*, *35*, 241-296, 1990.
- Oftedahl, C., Cauldrons of the Permian Oslo rift, *J. Volcanol. Geotherm. Res.*, *3*, 343-371, 1978.
- Poliakov, A.N.B., P. Cundall, Y. Podladchikov, and V. Laykhovsky, An explicit inertial method for the simulation of visco-elastic flow: An evaluation of elastic effects on diapiric flow in two- and three-layers models, in *Flow and Creep in the Solar System: Observations, Modelling and Theory, Dynamic Modelling and Flow in the Earth and Planets*, edited by D.B. Stone and S.K. Runcorn, pp. 175-195, Kluwer, Norwell, Mass., 1993a.
- Poliakov, A.N.B., Y. Podladchikov, and C. Talbot, Initiation of salt diapirs with frictional overburden: Numerical experiments, *Tectonophysics*, *228*, 199-210, 1993b.
- Poliakov, A., H.J. Hermann, Y. Podladchikov, and S. Roux, Fractal plastic shear bands, *Fractals*, *2*, 567-581, 1994.
- Ryan, M.P., Neutral buoyancy and the mechanical evolution of magmatic systems, in *Magmatic Processes: Physico-chemical Principles*, edited by B.O. Mysen, *Spec. Publ. Geochem. Soc.*, *1*, 259-287, 1987.
- Rytuba, J.J., Evolution of volcanic and tectonic features in caldera settings and their importance in the localization of ore deposits, *Econ. Geol.*, *89*, 1687-1696, 1994.
- Rytuba, J.J., A. Arribas Jr., C.G. Cunningham, E.H. McKee, M.H. Podwysoki, J.G. Smith, W.C. Kelly, and A. Arribas, Mineralized and unmineralized calderas in Spain, part II, Evolution of the Rodalquilar caldera complex and associated gold-alunite deposits, *Miner. Deposita*, *25*, S29-S35, 1990.
- Sibson, R.H., Earthquake rupturing as a mineralizing agent in hydrothermal systems, *Geology*, *15*, 701-704, 1987.
- Sillitoe, R.H., Erosion and collapse of volcanoes: cause of telescoping in intrusion-centered ore deposits, *Geology*, *22*, 945-948, 1994.
- Smith, R.L., Ash flows, *Geol. Soc. Am. Bull.*, *71*, 795-842, 1960.
- Smith, R.L., and R.A. Bailey, Resurgent cauldrons, *Mem. Geol. Soc. Am.*, *116*, 83-104, 1968.
- Sorey, M.L., G.A. Suemnicht, N.C. Sturchio, and G.A. Nordquist, New evidence on the hydrothermal system in Long Valley caldera, California, from wells, fluid sampling, electrical geophysics, and age determinations of hot spring deposits, *J. Volcanol. Geotherm. Res.*, *48*, 229-263, 1991.
- Stephenson, R.A., S.M. Nakiboglu, and M. A. Kelly, Effects of asthenosphere melting, regional thermostasy, and sediment loading on the thermomechanical subsidence of extensional sedimentary basins, in *Origin and Evolution of Sedimentary Basins and their Energy and Mineral Resources*, *Geophys. Monogr. Ser.*, vol 48, edited by R.A. Price, pp. 17-27, AGU, Washington, D.C., 1989.
- Steven, T.A., and P.W. Lipman, Calderas of the San Juan volcanic field, southwestern Colorado, *U.S. Geol. Surv. Prof. Pap.*, *958*, 1-35, 1976.
- Strujkov, S.F., O.B. Ryjov, V.V. Aristov, N.V. Grygoriev, Y.I. Radchenko, A.G. Kolesnikov, and G.J. Abbott, Geological structure and ore mineralogy of the Julietta gold-silver deposit, Northeast Russia, *Int. Geol. Rev.*, *38*, 625-648, 1996.
- Timoshenko, S.P., and S. Woinowsky-Krieger, *Theory of Plates and Shells*, 580 pp., McGraw-Hill, New York, 1959.
- Troise, C., G. De Natale, F. Pingue, and A. Zollo, A model for earthquake generation during unrest episodes

- at Campi Flegrei and Rabaul calderas, *Geophys. Res. Lett.*, *24*, 1575-1578, 1997.
- Tsenn, M.C., and N.L. Carter, Flow properties of continental lithosphere, *Tectonophysics*, *136*, 27-63, 1987.
- Turcotte, D., and G. Schubert, *Geodynamics: Applications of Continuum Physics to Geological Problems*, 450 pp., Wiley, New York, 1982.
- van Wees, J.D., and S. Cloeting, 3D flexure and intraplate compression in the North Sea Basin, *Tectonophysics*, *266*, 343-359, 1996.
- Watts, A.B., An analysis of isostasy in the world's oceans, 1, Hawaiian-Emperor Seamount Chain, *J. Geophys. Res.*, *83*, 5989-6004, 1978.
- Williams, H., Calderas and their origin, *Univ. Calif. Publ. Geol. Sci.*, *25*, 239-346, 1941.

E. Burov, Tectonics Department, University of Pierre and Marie Curie, 4 place Jussieu, 75252 Paris Cedex 5, France. (burov@brgm.fr)

L. Guillou-Frottier, BRGM, Geology and Metallogeny Laboratory, 3 av. C. Guillemin, B.P. 6009, F-45060 Orléans Cedex 2, France. (l.guillou-frottier@brgm.fr)

(Received December 30, 1998; revised May 31, 1999; accepted June 23, 1999.)